was then determined. Use of the aforementioned chaotropic agents, however, resulted in no improvement of immunoblot signals (Fig. 1B, lanes 5–7). In fact, the signal intensities diminished somewhat, possibly due to the presence of phosphorylated tau bound to the walls of the tube after removing the chaotropic agents prior to loading onto the SDS–PAGE gels [14].

Although negative results were obtained following use of the aforementioned chemical denaturants and detergent, we demonstrated that oligomeric Aip2p/Dld2p could modify the conformation of pathogenic highly aggregated polypeptides such as rPrP in the beta form, alpha-synuclein, and Abeta (1–42) in the presence of ATP [13]. Hence, the pick bodies were pretreated with oligomeric Aip2p/Dld2p prior to loading onto SDS–PAGE gels. Surprisingly, immunoblot analyses of Y337F, Y332F, and Y332T demonstrated discrete bands stained with anti-tau AT8 and AT100 antibodies following pretreatment with oligomeric Aip2p/Dld2p (Fig. 2). In a serial dilution assay, 1/500 of 500 pick bodies (equivalent to 1 pick body) was detected (Fig. 2, upper panel, lanes 4–8; lower panel, lanes 2–10).

These immunoreactive bands migrated slightly faster than those associated with the 500 pick bodies processed without oligomeric Aip2p/Dld2p pretreatment (Fig. 2, upper panel, lane 2). One possible explanation is that pretreatment with oligomeric Aip2p/Dld2p might allow the detection of the phosphorylated form of 60 kDa tau (tau 60) [4–6], whereas only the phosphorylated form of 69 kDa tau (tau 69) is negligibly detected following boiling in Laemmli's sample buffer according to classical immunoblotting procedures. Whether the different tau isoform could account for the faster migration pattern observed remains to be determined.

Oligomeric Aip2p/Dld2p was also detected in the same reaction mixtures using anti-Aip2p/Dld2p antibody (Fig. 2, upper panel, lanes 12–16) but did not cross-react with anti-tau AT8 and AT100 antibodies (Fig. 2, upper panel, lane 10). It should be noted that a single pick body directly pretreated with oligomeric Aip2p/Dld2p was sufficient to yield an immunoblot signal (Fig. 2, lower panel, lane 13), indicating that pretreatment with oligomeric Aip2p/Dld2p enhanced the immunoblot signal by more than 100-fold. Transmission electron microscopy with uranyl acetate negative staining of laser-microdissected pick bodies (Fig. 3) revealed that they were untangled following treatment with oligomeric Aip2p/Dld2p, whereas the

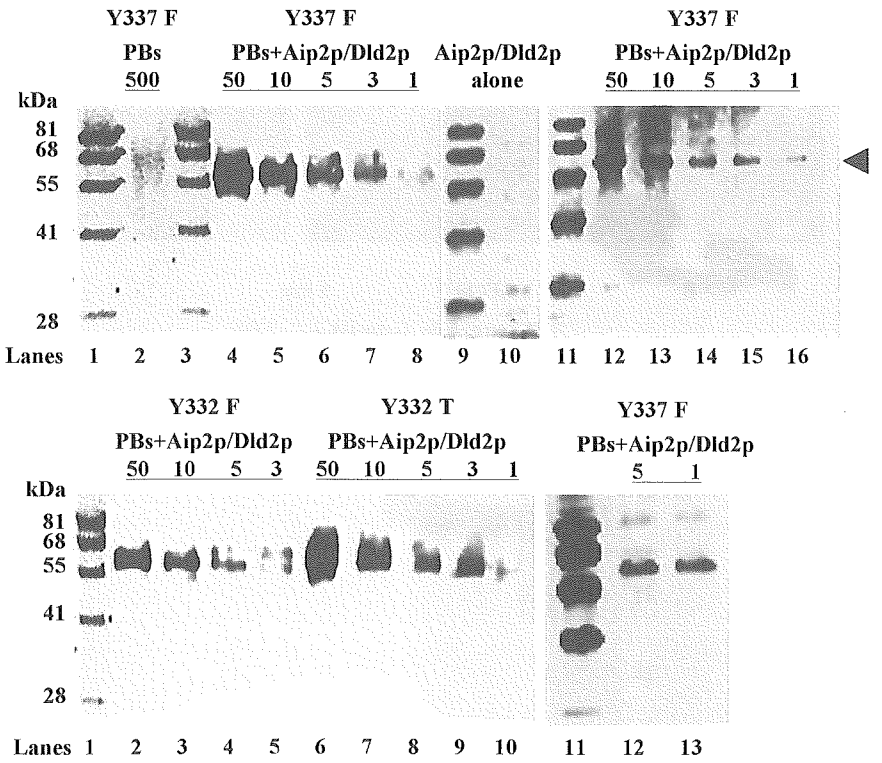

Fig. 2. Immunoblot analyses of laser-microdissected pick bodies (PBs) from Y337F (frontal cortex), Y332F (frontal cortex), and Y332T (temporal cortex). Upper panels: Molecular weight marker (Dr. Western, Oriental Yeast, lanes 1, 3, 9, and 11), 500 laser-microdissected PBs of Y337F (lane 2), and serial dilutions equivalent to 50, 10, 5, and 3 PBs and 1 PB of Y337F (lanes 4–8 and 12–16). Lane 2 represents sample without oligomeric Aip2p/Dld2p pretreatment, whereas lanes 4 to 8 and lanes 12 to 16 represent samples with oligomeric Aip2p/Dld2p pretreatment. Lane 10: 50 ng of Aip2p/Dld2p alone. Lanes 2, 4 to 8, and 10 were stained with anti-tau AT8 (1:1000) and AT100 (1:1000), whereas lanes 12 to 16 were stained with anti-Aip2p/Dld2p polyclonal antibody. The arrowhead indicates the position of Aip2p/Dld2p (MW = 58 kDa). Lower panels: Molecular weight marker (Dr. Western, Oriental Yeast, lanes 1 and 11), serial dilutions of 500 PBs of Y332F equivalent to 50, 10, 5, and 3 PBs (lanes 2–5), and those of Y332T equivalent to 50, 10, 5, and 3 PBs and 1 PB (lanes 6–10). Lanes 12 and 13: 5 PBs and 1 PB of Y337F, respectively. Samples in lower panels were pretreated with oligomeric Aip2p/Dld2p and stained with anti-tau AT8 (1:1000) and AT100 (1:1000).

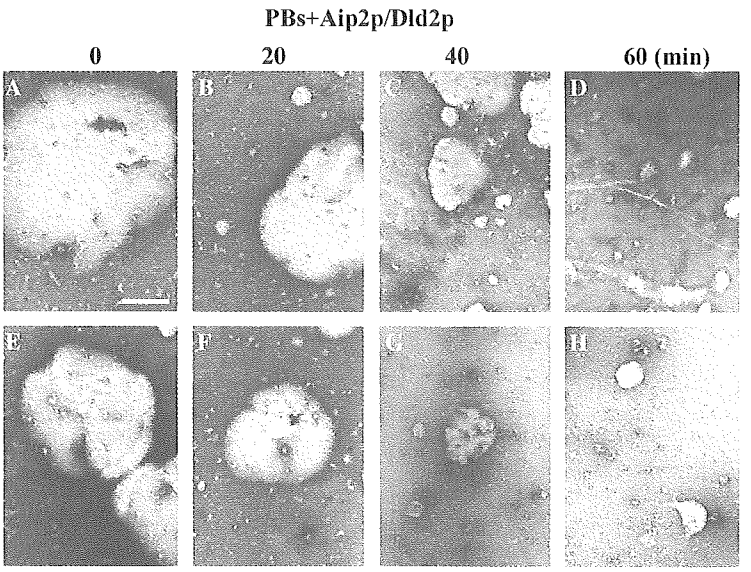

Fig. 3. Transmission electron microscopy with uranyl acetate negative staining of laser-microdissected pick bodies (PBs) prior to (A and E) and following oligomeric Aip2p/Dld2p pretreatment for 20 min (B and F), 40 min (C and G), and 60 min (D and H). For the negative staining, 500 PBs of Y332F were used as specimens. Scale bar is 4 μm.

average diameter of pick bodies decreased markedly, from 10 to 15 μm to less than 1 μm, in a time-dependent manner.

Although protein quantification of highly aggregated proteins such as pick bodies has been quite problematic to date, pretreatment with oligomeric Aip2p/Dld2p allows the ready quantification of the protein content of pick bodies (Table 1). The protein concentrations of sarkosyl-insoluble fractions were 0.8 ng (Y332T), 1.1 ng (Y332F), and 2.8 ng (Y337F) per 1 pick body. Because the average diameters of the pick bodies were 10 μm (Y332) and 15 μm (Y337), the relative densities of the pick bodies were 1.6 to 2.2 (Y332) and 1.6 (Y337).

Discussion

Our novel combinatorial method targets proteins relating to specific regions of interest at the micrometer order and exclusively allows the gathering of information pertaining to the molecular profile, such as molecular weight, of target proteins under the microscope in situ. During our investigations, we noticed that laser-microdissected pick bodies exhibited only faint and blurred immunoblot signals with anti-tau AT8 and AT100 antibodies, even following pretreatment with chemical denaturants or detergent, presumably resulting from the extensive aggregation property. In fact, this is extremely crucial when only a minimal quantity of target protein is available.

The protein conformation unfolding activity of oligomeric Aip2p/Dld2p can modify the conformation of pathogenic highly aggregated polypeptides [13]. Therefore, pick bodies were pretreated with oligomeric Aip2p/Dld2p to overcome the extensive aggregation property. With the pretreatment, 500 ng of oligomeric Aip2p/Dld2p (MW ~700 kDa) was mixed with 500 pick bodies consisting of abnormally phosphorylated tau (MW = 58 kDa), indicating that the stoichiometry of oligomeric Aip2p/Dld2p:phosphorylated tau is approximately 1:10. As shown in Fig. 2, oligomeric Aip2p/Dld2p pretreatment enhanced the immunoblot signals by more than 100-fold.

The inclusion bodies, which might protect against toxicity [15], have been associated with various protein conformation disorders, including Alzheimer's disease [16], Parkinson's disease [17], and prion disease (e.g., bovine spongiform encephalopathy) [18]. Actually, the robust protein conformation unfolding activity of oligomeric Aip2p/Dld2p modulated the conformation of Abeta (1–42) peptide associated with Alzheimer's disease, alpha-synuclein associated with Parkinson's disease, and rPrP in the beta form associated with prion disease in vitro [13]. Therefore, use of oligomeric Aip2p/Dld2p with our combinatorial method provides significant improvement in the investigation of normal or abnormal microstructures under various conditions and of disorders with extremely enhanced sensitivity.

Making use of this unprecedented property of oligomeric Aip2p/Dld2p may yield further potential applications. For example, a number of proteomic strategies rely on liquid chromatography–tandem mass spectrometry (LC–MS/MS), but sample preparation methods typically involve the use of detergents and chaotropic agents that often interfere with chromatographic separation and/or electrospray ionization [19]. Use of oligomeric Aip2p/Dld2p, however, would not interfere with the LC–MS/MS procedures and might even prove to be ideal for sample pretreatment. Overall, use of oligomeric Aip2p/Dld2p might significantly facilitate nano-scale analysis, which is often hindered by the aggregation property of target proteins present under various analytical conditions, especially when the sample protein is present in minor quantities.

Acknowledgments

We thank K. Watanabe and K. Takayama for technical assistance. This work was supported by grants from the Ministry of Health, Labor, and Welfare and the Ministry of Education, Culture, Sports, Science, and Technology, Japan, and from the Core Research for Evolutional Science and Technology (CREST) of Japan Science and Technology Agency.

References

[1] U.K. Laemmli, Cleavage of structural proteins during the assembly of the head of bacteriophage T4, Nature 227 (1970) 680–685.
[2] T. Tanaka, T. Ito, M. Furuta, C. Eguchi, H. Toda, E. Wakabayashi-Takai, K. Kaneko, In situ phage screening: a method for identification of subnanogram tissue components in situ, J. Biol. Chem. 277 (2002) 30382–30387.
[3] S. Hardin, B. Schooley, A story of Pick's disease: a rare form of dementia, J. Neurosci. Nurs. 34 (2002) 117–122.
[4] V. Zhukareva, D. Mann, S. Pickering-Brown, K. Uryu, T. Shuck, K. Shah, M. Grossman, B.L. Miller, C.M. Hulette, S.C. Feinstein, J.Q. Trojanowski, V.M. Lee, Sporadic Pick's disease: a tauopathy characterized by a spectrum of pathological tau isoforms in gray and white matter, Ann. Neurol. 51 (2002) 730–739.
[5] A. Delacourte, N. Sergeant, A. Wattez, D. Gauvreau, Y. Robitaille, Vulnerable neuronal subsets in Alzheimer's and Pick's disease are distinguished by their tau isoform distribution and phosphorylation, Ann. Neurol. 43 (1998) 193–204.
[6] T. Arai, K. Ikeda, H. Akiyama, Y. Shikamoto, K. Tsuchiya, S. Yagishita, T. Beach, J. Rogers, C. Schwab, P.L. McGeer, Distinct isoforms of tau aggregated in neurons and glial cells in brains of patients with Pick's disease, corticobasal degeneration, and progressive supranuclear palsy, Acta Neuropathol. (Berl.) 101 (2001) 167–173.
[7] W. Martinet, V. Abbeloos, N. Van Acker, G.R. De Meyer, A.G. Herman, M.M. Kockx, Western blot analysis of a limited number of cells: a valuable adjunct to proteome analysis of paraffin wax-embedded, alcohol-fixed tissue after laser capture microdissection, J. Pathol. 202 (2004) 382–388.
[8] D.C. Amberg, E. Basart, D. Botstein, Defining protein interactions with yeast actin in vivo, Nat. Struct. Biol. 2 (1995) 28–35.
[9] A. Chelstowska, Z. Liu, Y. Jia, D. Amberg, R.A. Butow, Signalling between mitochondria and the nucleus regulates the expression of a new D-lactate dehydrogenase activity in yeast, Yeast 15 (1999) 1377–1391.
[10] M.J. Flick, S.F. Konieczny, Identification of putative mammalian D-lactate dehydrogenase enzymes, Biochem. Biophys. Res. Commun. 295 (2002) 910–916.
[11] N.S. Hachiya, Y. Sakasegawa, A. Jozuka, S. Tsukita, K. Kaneko, Interaction of D-lactate dehydrogenase protein 2 (Dld2p) with F-actin: Implication for an alternative function of Dld2p, Biochem. Biophys. Res. Commun. 319 (2004) 78–82.
[12] N.S. Hachiya, Y.H.S. Sakasegawa, A. Jozuka, S. Tsukita, K. Kaneko, Oligomeric Aip2p/Dld2p forms a novel grapple-like structure and has an ATP-dependent F-actin conformation modifying activity in vitro, Biochem. Biophys. Res. Commun. 320 (2004) 1271–1276.
[13] N.S. Hachiya, Y.H.S. Sakasegawa, A. Jozuka, S. Tsukita, K. Kaneko, Oligomeric Aip2p/Dld2p modifies the protein conformation of both properly-folded and misfolded substrates in vitro, Biochem. Biophys. Res. Commun. 323 (2004) 339–344.
[14] K. Kaneko, D. Peretz, K.M. Pan, T.C. Blochberger, H. Wille, R. Gabizon, O.H. Griffith, F.E. Cohen, M.A. Baldwin, S.B. Prusiner, Prion protein (PrP) synthetic peptides induce cellular PrP to acquire properties of the scrapie isoform, Proc. Natl. Acad. Sci. USA 92 (1995) 11160–11164.
[15] M. Tanaka, Y.M. Kim, G. Lee, E. Junn, T. Iwatsubo, M.M. Mouradian, Aggresomes formed by alpha-synuclein and synphilin-1 are cytoprotective, J. Biol. Chem. 279 (2004) 4625–4631.
[16] J.W. Lustbader, M. Cirilli, C. Lin, H.W. Xu, K. Takuma, N. Wang, C. Caspersen, X. Chen, S. Pollak, M. Chaney, F. Trinchese, S. Liu, F. Gunn-Moore, L.F. Lue, D.G. Walker, P. Kuppusamy, Z.L. Zewier, O. Arancio, D. Stern, S.S. Yan, H. Wu, ABAD directly links Abeta to mitochondrial toxicity in Alzheimer's disease, Science 304 (2004) 448–452.
[17] J.T. Greenamyre, T.G. Hastings, Parkinson's: divergent causes, convergent mechanisms, Science 304 (2004) 1120–1122.
[18] M.P. Mayer, H. Schroder, S. Rudiger, K. Paal, T. Laufen, B. Bukau, Multistep mechanism of substrate binding determines chaperone activity of Hsp70, Nat. Struct. Biol. 7 (2000) 586–593.
[19] J. Blonder, M.B. Goshe, R.J. Moore, L. Pasa-Tolic, C.D. Masselon, M.S. Lipton, R.D. Smith, Enrichment of integral membrane proteins for proteomic analysis using liquid chromatography–tandem mass spectrometry, J. Proteome Res. 1 (2002) 351–360.

Available online at www.sciencedirect.com
SCIENCE DIRECT®
ELSEVIER
Biochemical and Biophysical Research Communications 338 (2005) 1229–1235
BBRC
www.elsevier.com/locate/ybbrc

siRNA-mediated inhibition of endogenous Huntington disease gene expression induces an aberrant configuration of the ER network in vitro

Kazuya Omi [a,b], Naomi S. Hachiya [a], Katsushi Tokunaga [b], Kiyotoshi Kaneko [a,*]

[a] *Second Department of Physiology, Tokyo Medical University, Tokyo 160-8402, Japan*
[b] *Department of Human Genetics, Graduate School of Medicine, The University of Tokyo, Tokyo 113-0033, Japan*

Received 5 October 2005
Available online 21 October 2005

Abstract

Huntingtin is a ubiquitously expressed cytoplasmic protein encoded by the Huntington disease (HD) gene, in which a CAG expansion induces an autosomal dominant progressive neurodegenerative disorder; however, its biological function has not been completely elucidated. Here, we report for the first time that short interfering RNA (siRNA)-mediated inhibition of endogenous Hdh (a mouse homologue of huntingtin) gene expression induced an aberrant configuration of the endoplasmic reticulum (ER) network in vitro. Studies using immunofluorescence microscopy with several ER markers revealed that the ER network appeared to be congregated in various types of cell lines transfected with siRNA directed against Hdh, but not with other siRNAs so far tested. Other subcellular organelles and structures, including the nucleus, Golgi apparatus, mitochondria, lysosomes, microtubules, actin cytoskeletons, cytoplasm, lipid rafts, and plasma membrane, exhibited normal configurations. Western blot analysis of cellular prion protein (PrP^C) revealed normal glycosylation, which is a simple marker of post-translational modification in the ER and Golgi compartments, and immunofluorescence microscopy detected no altered subcellular distribution of PrP^C in the post-ER compartments. Further investigation is required to determine whether the distorted ER network, i.e., loss of the huntingtin function, participates in the development of HD.

Keywords: Huntingtin; Huntington disease; Mouse homologue of huntingtin; Short interfering RNA; Endoplasmic reticulum; Microtubules

Huntingtin [1] is a ubiquitously expressed 348-kDa cytoplasmic protein encoded by the Huntington disease (HD) gene. A CAG expansion in this gene induces an autosomal dominant progressive neurodegenerative disorder characterized by the appearance of progressive chorea and dementia, usually in adult life [2]. Since the cloning of the HD gene in 1993, most efforts directed toward understanding the pathogenic mechanism of this disease have focused on the analyses of the mutant huntingtin; the basis of these analyses is the gain-of-function hypothesis. However, the biological function of huntingtin has not been fully elucidated [3].

Recent studies have indicated that wild-type huntingtin is essential for embryonic development and normal function in adulthood [4]. Several independent studies using knockout mice that do not express a mouse homologue of the HD (Hdh) gene demonstrated that wild-type huntingtin plays a crucial role in embryogenesis because, in all cases, nullizygous mouse embryos died at approximately embryonic day E7.5 [5–7]. Alternatively, conditional inactivation of wild-type huntingtin resulted in neurological deficits and neurodegeneration, indicating the importance of the wild-type huntingtin function in adulthood [8].

Although a number of techniques, including an antisense method [9,10] and a catalytic DNA strategy [11], have been used to inhibit huntingtin expression, their efficiency is quite low. On the other hand, short interfering RNA (siRNA) has proven to be a much more powerful tool for

* Corresponding author. Fax: +81 3 3351 6544.
E-mail address: k-kaneko@tokyo-med.ac.jp (K. Kaneko).

0006-291X/$ - see front matter © 2005 Elsevier Inc. All rights reserved.
doi:10.1016/j.bbrc.2005.10.061

suppressing the expression of genes of interest in various mammalian cells [12,13]. Indeed, several groups have reported the suppression of human HD transgene using siRNA [14–16]; however, these studies did not examine loss of endogenous Hdh function.

In order to collect information on its physiological function, we inhibited endogenous Hdh expression using siRNA and examined the morphology of subcellular organelles including the nucleus, endoplasmic reticulum (ER), Golgi apparatus, mitochondria, lysosomes, microtubules, actin cytoskeletons, cytoplasm, lipid rafts, and plasma membrane in various cultured cells. Consequently, the siRNA-mediated inhibition of endogenous Hdh expression induced an aberrant configuration of the ER network with no remarkable secretion deficit in vitro.

Materials and methods

Synthetic siRNA duplexes. siRNAs against the Hdh gene were designed using the algorithm proposed by Naito et al. [17]. The sense strand sequences of newly synthesized siRNA were as follows: siHdh1, 5′-CCGUGUGAA UCAUUGUCUAAC-3′; siHdh2, 5′-GGAGCAUCGUGGAGCUUUU AG-3′; and control (non-silencing) siRNA, 5′-UUCUCCGAACCUGUCA CGUUU-3′. The *Photinus* luciferase (La2 [18]), green fluorescent protein (GFP, Qiagen, Hilden, Germany), amyloid precursor protein (APP, Ambion, Austin, TX, USA), and glyceraldehyde-3-phosphate dehydrogenase (GAPDH, Ambion, Austin, TX, USA) siRNAs were purchased and used. For preparation of siRNA duplexes, sense- and antisense-stranded oligonucleotides were mixed in an annealing buffer (30 μM Hepes, pH 7.4; 100 μM potassium acetate; and 2 μM magnesium acetate), heat denatured at 95 °C for 5 min, and annealed at 37 °C overnight.

Cell culture and transfection. Mouse neuroblastoma neuro2a (N2a) and human glioblastoma T98G cells were obtained from the American Tissue Culture Collection. N2a cells were grown and maintained at 37 °C in minimum essential medium (MEM) supplemented with 10% fetal bovine serum (FBS). T98G cells were grown and maintained at 37 °C in Dulbecco's modified Eagle's medium (DMEM) supplemented with 10% FBS. Synthetic siRNA duplexes (40 nM) were transfected into N2a cells by using jetSI (Qbiogene, Irvine, CA, USA) and into T98G cells by using Lipofectamine 2000 (Invitrogen, Carlsbad, CA, USA) reagents.

Real-time PCR. After the transfection of siRNA duplexes, total RNA was extracted with Trizol (Invitrogen, Carlsbad, CA, USA) and subjected to cDNA synthesis by using oligo(dT) primers and a SuperScript II reverse transcriptase (Invitrogen, Carlsbad, CA, USA). The resultant cDNAs were examined by real-time PCR using the ABI 7000 sequence detection system (Applied Biosystems, Foster City, CA, USA) with a SYBR Green PCR Master Mix (Applied Biosystems, Foster City, CA, USA) and a TaqMan Assay-on-Demand Gene Expression Product (Applied Biosystems, Foster City, CA, USA) for the mouse GAPDH gene that functioned as a control, according to the manufacturer's instructions. The PCR primers for detection of the Hdh transcript were as follows: Mm.Hdh-F, 5′-TTCTGCTTGAATTGTACAGC-3′ and Mm.Hdh-R, 5′-AATGAGG ATCTCATCTTCTG-3′. The expression level of the Hdh gene was normalized to that of the GAPDH gene.

Antibodies and organelle markers. Anti-huntingtin antibody MAB2166 was purchased from Chemicon (Temecula, CA, USA). As ER markers, anti-Calnexin (Stressgen, San Diego, CA, USA), anti-PDI antibody (Stressgen, San Diego, California, USA), ER-Tracker Blue-White DPX (Molecular Probes, Carlsbad, CA, USA), and pECFP-ER (Clontech, Mountain View, CA, USA) were purchased and used. Other organelle markers, including a nuclear marker, DAPI (Molecular Probes, Carlsbad, CA, USA); a Golgi marker, anti-GM130 antibody (BD Biosciences, San Jose, CA, USA); a mitochondrial marker, MitoTracker Red CMXROS (Molecular Probes, Carlsbad, CA, USA) and anti-porin antibody (Calbiochem, San Jose, CA, USA); a lysosomal marker, LysoTracker Red (Molecular Probes, Carlsbad, CA, USA); a marker for microtubules, anti-tubulin antibody DM1A (Sigma, Tokyo, Japan); a marker for actin cytoskeleton, rhodamine phalloidin (Molecular Probes, Carlsbad, CA, USA); a cytoplasmic marker, anti-Hsp70 antibody (BD Biosciences, San Jose, CA, USA); a marker for lipid rafts, anti-GM1 antibody (Chemicon, Temecula, CA, USA); a plasma membrane marker, FM 1-43FX (Molecular Probes, Carlsbad, CA, USA); and a microsome marker, anti-Erp57 antibody (Stressgen, San Diego, CA, USA) were also used for the experiments. Anti-prion protein (PrP) antibody SAF-32 was purchased from Cayman Chemical (Michigan, USA). Western blot analyses were performed as described [19].

Immunofluorescence and fluorescence microscopy. For indirect immunofluorescence analysis, cells with siRNAs were rinsed with phosphate-buffered saline (PBS) Ca^{2+} and Mg^{2+} (PBS(+)) and then fixed with 10% formalin in 70% PBS(+). After four washes with PBS(−), the fixed cells were incubated with 10 % FBS in PBS(−) at room temperature for 30 min. They were then incubated at room temperature for 1 h with primary antibodies at the desired concentration. After four washes with PBS(−), the cells were incubated with Alexa 488 Fluor-conjugated anti-mouse or anti-rabbit IgG (Molecular Probes, Carlsbad, CA, USA), diluted 1:100 in PBS, at room temperature for 2.5 h. The stained cells were washed four times with PBS(−) and mounted with SLOW FADE (Molecular Probes, Carlsbad, CA, USA). Immunofluorescent or autofluorescent samples were imaged using a DeltaVision microscopy system (Applied Precision, Washington, USA); out of focus light of the visualized images was eliminated by interactive deconvolution.

Preparation of mitochondrial, microsome, and cytosolic fractions [20] Cells were homogenized with 4 volumes of homogenize buffer (10 mM Hepes–KOH, pH 7.4, 250 mM sucrose, 1 mM EDTA, and 1 mM DTT) and centrifuged at 800*g* for 5 min at 4 °C, and the supernatant was further centrifuged at 8000*g* for 5 min at 4 °C. The supernatant was used as a post-mitochondrial supernatant. The resulted pellet was washed three times with homogenize buffer, resuspended in 4 volumes of the same buffer, and then centrifuged at 5000*g* for 10 min at 4 °C. The pellet was recovered and used as mitochondrial fraction. The post-mitochondrial supernatant was further centrifuged at 100,000*g* for 1 h at 4 °C, and the supernatant was used as cytosolic fraction, and the pellet was resuspended in homogenize buffer (microsome fraction). Western blots were performed at 3 μg of total protein/lane.

Results

siHdh1 and siHdh2 inhibit endogenous Hdh expression in vitro

In vitro screening was used to identify an effective siRNA directed against endogenous Hdh mRNA. Two siRNAs (siHdh1 and siHdh2) reduced endogenous Hdh mRNA levels by 75% and 60%, respectively, in comparison with those in the control siRNA-treated mouse N2a cells (Fig. 1A). After the transfection with siHdh1 or siHdh2 in N2a cells, Western blot analysis with an anti-huntingtin antibody (MAB2166) revealed a significant reduction in endogenous Hdh expression (Fig. 1B), of which the subcellular localization was predominantly in a microsome fraction using a subcellular fractionation method (Fig. 1C).

siHdh1-mediated inhibition of endogenous Hdh expression induces an aberrant configuration of the ER network in vitro

After siHdh1 was introduced into mouse N2a cells, immunofluorescence and fluorescence studies were performed.

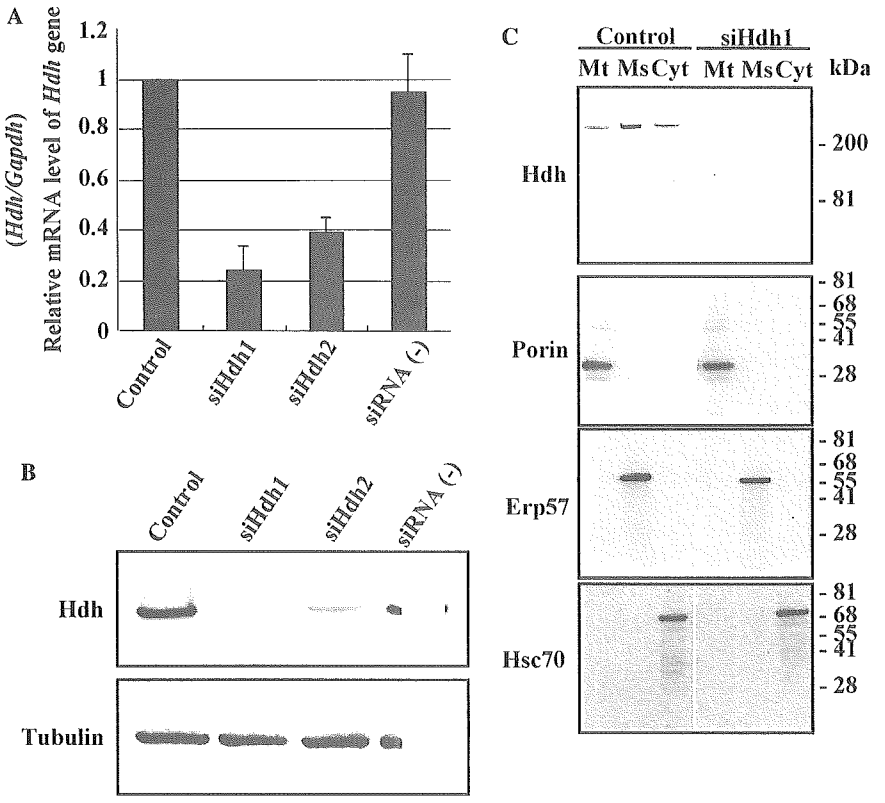

Fig. 1. Significant reduction of endogenous Hdh expression in siHdhl- or siHdh2-transfected mouse N2a cells. (A) Quantitative real-time PCR analyses of endogenous Hdh mRNA levels relative to endogenous GAPDH mRNA in N2a cells transfected with siHdh1 or siHdh2. (B) Western blot analysis of endogenous Hdh expression using an anti-huntingtin antibody (MAB2166, 1:2000) in N2a cells transfected with siHdh1 or siHdh2. Tubulin is used as an internal control. (C) Subcellular distribution of endogenous Hdh by Western blot analysis with an anti-huntingtin antibody (MAB2166, 1:2000) in N2a cells transfected with siHdh1. Anti-porin antibody as a mitochondrial (Mt) marker, anti-Erp57 antibody as a microsome (Ms) marker, and anti-Hsp70 antibody as a cytosolic (Cyt) marker were used at 1:1000.

Interestingly, immunofluorescence microscopy with an ER marker (anti-calnexin) revealed that siHdh1-mediated inhibition of endogenous Hdh expression induced an aberrant configuration of the ER network that appeared to be congregated (Fig. 2A). Immunofluorescence studies with other ER markers including anti-PDI, ER tracker Blue-White DPX, and pECFP-ER produced similar results (Fig. 2B). However, other subcellular organelles including the nucleus, Golgi apparatus, mitochondria, lysosomes, microtubules, actin cytoskeletons, cytoplasm, lipid rafts, and plasma membrane exhibited no comparable morphological alteration in these cells (Fig. 2A). In addition, siHdh2 directed against a different region of the Hdh gene sequence also induced a similar distortion of the ER network, whereas no distortion was induced by other siRNAs such as siGFP directed against GFP, siGAPDH directed against GAPDH, siLa2 directed against *Photinus* luciferase, or siAPP directed against APP (Fig. 2C).

siHdh1-mediated aberrant configuration of the ER network in a different cell line

The potential to inhibit endogenous Hdh expression was first analyzed by the transfection of siHdh1 into different cell lines. As evaluated by Western blot analyses, siHdh1 induced a significant reduction of Hdh expression level in human glioblastoma T98G cells (Fig. 2D). The aberrant configuration of the ER network was once again observed in these cells (Fig. 2D).

Normal glycosylation and subcellular distribution of endogenous cellular prion protein in siHdh1-transfected N2a cells

Cellular prion protein (PrP^C) is a glycosyl phosphatidylinositol-anchored secretary glycoprotein that resides predominantly in the Golgi apparatus and to a lesser extent on the plasma membrane [21,22]. In order to further examine whether siHdh1-mediated endogenous Hdh inhibition induces any functional alteration associated with the aberrant configuration of the ER network, endogenous PrP^C was chosen; its glycosylation pattern, which is a simple marker of the post-translational modification in the ER and Golgi compartments, as well as its subcellular distribution profile were further investigated for 72 h. Western blot analysis using the anti-PrP antibody SAF-32 revealed normal glycosylation of endogenous PrP^C in N2a cells transfected with either siHdh1 or siHdh2 (Fig. 3A). Similarly,

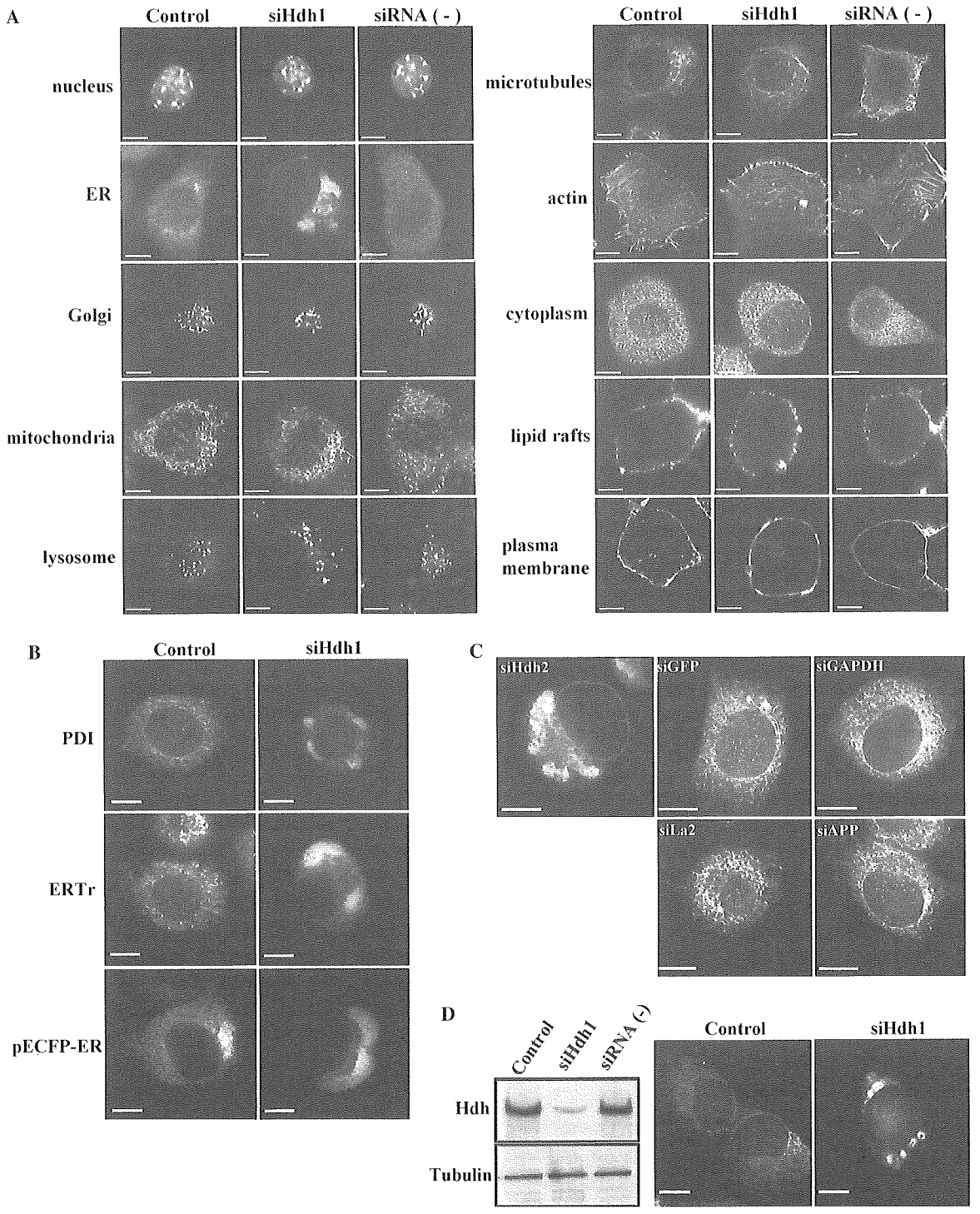

Fig. 2. Subcellular distribution profile of organelles in siHdh1-transfected N2a cells. (A) Immunofluorescence microscopy with an anti-ER antibody (anti-calnexin, 1:200) detects an aberrant configuration of the ER network that appears to be congregated in the siHdh1-transfected N2a cells. Other organelles, including the nucleus (DAPI, 0.5 μg/ml), Golgi (anti-GM130 antibody, 1:100), mitochondria (MitoTracker Red CMXROS, 0.2 μg/ml), lysosomes (LysoTracker Red, 0.5 μg/ml), microtubules (anti-tubulin antibody DM1A, 1:100), actin (rhodamine phalloidin, 1:100), cytoplasm (anti-Hsp70 antibody, 1:100), lipid rafts (anti-GM1 antibody, 1:100), and plasma membrane (FM 1-43FX, 0.5 μg/ml), exhibit no comparable morphological alteration. Scale bars are 3.5 μm. (B) Immunofluorescence and fluorescence microscopy with other ER markers, including anti-PDI antibody (1:100), ER tracker Blue-White DPX (ERTr, 0.4 μg/ml), and pECFP-ER (1 μg of plasmid DNA was transfected) in the same cells. Scale bars are 5 μm. (C) siHdh2 also induces a similar distortion of the ER network in N2a cells, whereas no distortion is induced by other siRNAs, including siGFP directed against GFP, siGAPDH directed against GAPDH, siLa2 directed against La2, or siAPP directed against APP. Scale bars are 5 μm. (D) siHdh1-mediated aberrant configuration of the ER network in human glioblastoma T98G cells. Western blot analysis of endogenous Hdh expression levels in the T98G cells. The ER network is distorted and appears to be congregated in the cells after transfection with siHdh1. Anti-calnexin antibody (1:200) is used as an ER marker. Scale bars are 5 μm.

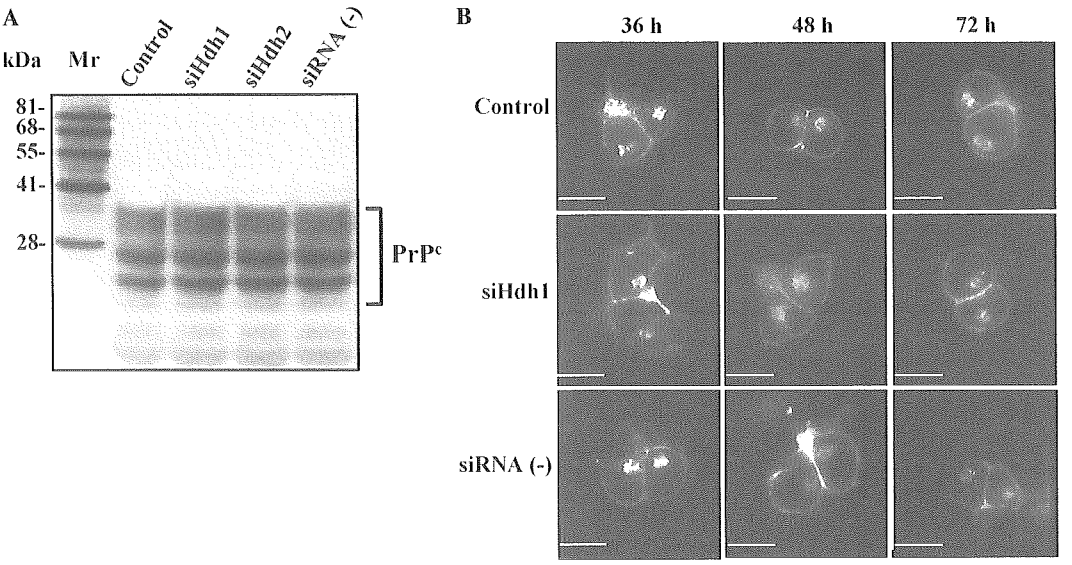

Fig. 3. Normal glycosylation and subcellular localization of endogenous PrP^C in post-ER compartments. (A) Western blot analysis using the anti-PrP antibody SAF-32 (1:5000). Transfection of siHdh1 or siHdh2 induces normal glycosylation pattern of endogenous PrP^C in N2a cells. M_r, molecular weight marker. (B) Immunofluorescence microscopy with the anti-PrP antibody SAF-32 (1:100). Transfection of siHdh1 induces no remarkable alteration of the subcellular distribution profile of endogenous PrP^C in N2a cells, where PrP^C resides predominantly in the Golgi apparatus and to a lesser extent on the plasma membrane. Scale bars are 15 μm.

no alteration of its subcellular distribution was detected by immunofluorescence microscopy in the post-ER compartments of siHdh1-transfected N2a cells (Fig. 3B).

Discussion

Huntingtin is located in neurons throughout the brain and the highest levels are observed in larger neurons [23]. The subcellular localization of huntingtin is consistent with that of a cytoplasmic protein [24,25]. Previous in vitro studies indicated that in mammalian neurons, wild-type huntingtin is involved in fast axonal trafficking [26,27], transcription, and vesicular transport of brain-derived neurotrophic factor along microtubules [28,29]. Huntingtin has also been reported to be involved in protection from toxic stresses, including those caused by a variety of apoptotic stimuli and the mutant huntingtin fragment [30,31], and in neuronal Ca^{2+} signaling, where it is associated with $InsP_3R$, an intracellular calcium release channel in the ER membrane [32]. However, no investigation has ever indicated the morphological alteration of subcellular organelles in the endogenous huntingtin-deleted condition; thus, this is the first report suggesting that huntingtin might be involved in maintaining the proper configuration of the ER network.

The dynamics of the ER network depends on a cytoskeletal system of microtubules. Colocalization of ER networks with microtubules has been described in various mammalian cell lines [33,34]. Prolonged depolymerization of microtubules by nocodazole treatment leads to a slow retraction of the ER network towards the cell center, indicating that the extended state of the entire ER network requires the microtubule system [33]. By using dynamic imaging techniques on living cells treated with a fluorescent ER marker, Lee et al. categorized and analyzed several distinct forms of highly localized ER movements, suggesting that microtubules may play a role in generating ER motility and in constructing and maintaining the ER network [33,34].

When considered together, huntingtin appears to modulate the configuration of the ER network via the cytoskeletal network, particularly through the microtubular network [23]. The fact that most of the huntingtin in the cytoplasm is associated with assembled microtubules supports this notion [35]. Considering the other fact that the microtubular network was not affected by siRNA-mediated inhibition of Hdh expression whereas the intracellular distribution of the ER network was severely altered, huntingtin appears to play a significant role in maintaining the ER network but not the microtubular network, probably because the maintenance of the latter is driven by other microtubule-associated proteins (MAPs) [36,37]. Further, the microtubular network is ubiquitous and also fundamental to various types of intracellular trafficking events [38,39]. Hence, further investigation is required to elucidate the mechanism by which huntingtin interacts with the microtubules that exclusively lead to the aberrant configuration of the ER network.

Finally, it is of great interest to determine whether the distorted ER network, i.e., loss of the huntingtin function is involved in the development of HD in vivo; this is because the the gain-of-function hypothesis has been proposed for the development of this disease.

Acknowledgments

We thank K. Watanabe and K. Takayama for technical assistance. This work was supported by grants

from the Ministry of Agriculture, Forestry and Fisheries and the Ministry of Health, Labor and Welfare of Japan.

References

[1] The Huntington's Disease Collaborative Research Group, A novel gene containing a trinucleotide repeat that is expanded and unstable on Huntington's disease chromosomes, Cell 72 (1993) 971–983.
[2] P.M. Conneally, Huntington disease: genetics and epidemiology, Am. J. Hum. Genet. 36 (1984) 506–526.
[3] P. Harjes, E.E. Wanker, The hunt for huntingtin function: interaction partners tell many different stories, Trends Biochem. Sci. 28 (2003) 425–433.
[4] E. Cattaneo, D. Rigamonti, D. Goffredo, C. Zuccato, F. Squitieri, S. Sipione, Loss of normal huntingtin function: new developments in Huntington's disease research, Trends Neurosci. 24 (2001) 182–188.
[5] M.P. Duyao, A.B. Auerbach, A. Ryan, F. Persichetti, G.T. Barnes, S.M. McNeil, P. Ge, J.P. Vonsattel, J.F. Gusella, A.L. Joyner, et al., Inactivation of the mouse Huntington's disease gene homolog Hdh, Science 269 (1995) 407–410.
[6] J. Nasir, S.B. Floresco, J.R. O'Kusky, V.M. Diewert, J.M. Richman, J. Zeisler, A. Borowski, J.D. Marth, A.G. Phillips, M.R. Hayden, Targeted disruption of the Huntington's disease gene results in embryonic lethality and behavioral and morphological changes in heterozygotes, Cell 81 (1995) 811–823.
[7] S. Zeitlin, J.P. Liu, D.L. Chapman, V.E. Papaioannou, A. Efstratiadis, Increased apoptosis and early embryonic lethality in mice nullizygous for the Huntington's disease gene homologue, Nat. Genet. 11 (1995) 155–163.
[8] I. Dragatsis, M.S. Levine, S. Zeitlin, Inactivation of Hdh in the brain and testis results in progressive neurodegeneration and sterility in mice, Nat. Genet. 26 (2000) 300–306.
[9] R.J. Boado, A. Kazantsev, B.L. Apostol, L.M. Thompson, W.M. Pardridge, Antisense-mediated down-regulation of the human huntingtin gene, J. Pharmacol. Exp. Ther. 295 (2000) 239–243.
[10] C. Nellemann, K. Abell, A. Norremolle, T. Lokkegaard, B. Naver, C. Ropke, J. Rygaard, S.A. Sorensen, L. Hasholt, Inhibition of Huntington synthesis by antisense oligodeoxynucleotides, Mol. Cell Neurosci. 16 (2000) 313–323.
[11] L. Yen, S.M. Strittmatter, R.G. Kalb, Sequence-specific cleavage of Huntingtin mRNA by catalytic DNA, Ann. Neurol. 46 (1999) 366–373.
[12] D.M. Dykxhoorn, C.D. Novina, P.A. Sharp, Killing the messenger: short RNAs that silence gene expression, Nat. Rev. Mol. Cell. Biol. 4 (2003) 457–467.
[13] K. Omi, K. Tokunaga, H. Hohjoh, Long-lasting RNAi activity in mammalian neurons, FEBS Lett. 558 (2004) 89–95.
[14] S.Q. Harper, P.D. Staber, X. He, S.L. Eliason, I.H. Martins, Q. Mao, L. Yang, R.M. Kotin, H.L. Paulson, B.L. Davidson, RNA interference improves motor and neuropathological abnormalities in a Huntington's disease mouse model, Proc. Natl. Acad. Sci. USA 102 (2005) 5820–5825.
[15] B. Huang, S. Kochanek, Adenovirus-mediated silencing of huntingtin expression by shRNA, Hum. Gene Ther. 16 (2005) 618–626.
[16] E. Rodriguez-Lebron, E.M. Denovan-Wright, K. Nash, A.S. Lewin, R.J. Mandel, Intrastriatal rAAV-mediated delivery of anti-huntingtin shRNAs induces partial reversal of disease progression in R6/1 Huntington's disease transgenic mice, Mol. Ther. (2005).
[17] Y. Naito, T. Yamada, K. Ui-Tei, S. Morishita, K. Saigo, siDirect: highly effective, target-specific siRNA design software for mammalian RNA interference, Nucleic Acids Res. 32 (2004) W124–W129.
[18] H. Hohjoh, RNA interference (RNA(i)) induction with various types of synthetic oligonucleotide duplexes in cultured human cells, FEBS Lett. 521 (2002) 195–199.
[19] M.R. Scott, R. Kohler, D. Foster, S.B. Prusiner, Chimeric prion protein expression in cultured cells and transgenic mice, Protein Sci. 1 (1992) 986–997.
[20] N.S. Hachiya, M. Yamada, K. Watanabe, A. Jozuka, T. Ohkubo, K. Sano, Y. Takeuchi, Y. Kozuka, Y. Sakasegawa, K. Kaneko, Mitochondrial localization of cellular prion protein (PrPC) invokes neuronal apoptosis in aged transgenic mice overexpressing PrPC, Neurosci. Lett. 374 (2005) 98–103.
[21] S.B. Prusiner, Molecular biology and transgenetics of prion diseases, Crit. Rev. Biochem. Mol. Biol. 26 (1991) 397–438.
[22] S.B. Prusiner, P. Peters, K. Kaneko, A. Taraboulos, V. Lingappa, F.E. Cohen, S.J. DeArmond, in: S.B. Prusiner (Ed.), Cell Biology of Prions, Cold Spring Harbor, New York, 1999.
[23] C.A. Gutekunst, A.I. Levey, C.J. Heilman, W.L. Whaley, H. Yi, N.R. Nash, H.D. Rees, J.J. Madden, S.M. Hersch, Identification and localization of huntingtin in brain and human lymphoblastoid cell lines with anti-fusion protein antibodies, Proc. Natl. Acad. Sci. USA 92 (1995) 8710–8714.
[24] M. DiFiglia, E. Sapp, K. Chase, C. Schwarz, A. Meloni, C. Young, E. Martin, J.P. Vonsattel, R. Carraway, S.A. Reeves, et al., Huntingtin is a cytoplasmic protein associated with vesicles in human and rat brain neurons, Neuron 14 (1995) 1075–1081.
[25] A.H. Sharp, S.J. Loev, G. Schilling, S.H. Li, X.J. Li, J. Bao, M.V. Wagster, J.A. Kotzuk, J.P. Steiner, A. Lo, et al., Widespread expression of Huntington's disease gene (IT15) protein product, Neuron 14 (1995) 1065–1074.
[26] J. Block-Galarza, K.O. Chase, E. Sapp, K.T. Vaughn, R.B. Vallee, M. DiFiglia, N. Aronin, Fast transport and retrograde movement of huntingtin and HAP 1 in axons, Neuroreport 8 (1997) 2247–2251.
[27] E. Trushina, R.B. Dyer, J.D. Badger II, D. Ure, L. Eide, D.D. Tran, B.T. Vrieze, V. Legendre-Guillemin, P.S. McPherson, B.S. Mandavilli, B. Van Houten, S. Zeitlin, M. McNiven, R. Aebersold, M. Hayden, J.E. Parisi, E. Seeberg, I. Dragatsis, K. Doyle, A. Bender, C. Chacko, C.T. McMurray, Mutant huntingtin impairs axonal trafficking in mammalian neurons in vivo and in vitro, Mol. Cell. Biol. 24 (2004) 8195–8209.
[28] L.R. Gauthier, B.C. Charrin, M. Borrell-Pages, J.P. Dompierre, H. Rangone, F.P. Cordelieres, J. De Mey, M.E. MacDonald, V. Lessmann, S. Humbert, F. Saudou, Huntingtin controls neurotrophic support and survival of neurons by enhancing BDNF vesicular transport along microtubules, Cell 118 (2004) 127–138.
[29] C. Zuccato, A. Ciammola, D. Rigamonti, B.R. Leavitt, D. Goffredo, L. Conti, M.E. MacDonald, R.M. Friedlander, V. Silani, M.R. Hayden, T. Timmusk, S. Sipione, E. Cattaneo, Loss of huntingtin-mediated BDNF gene transcription in Huntington's disease, Science 293 (2001) 493–498.
[30] D. Rigamonti, J.H. Bauer, C. De-Fraja, L. Conti, S. Sipione, C. Sciorati, E. Clementi, A. Hackam, M.R. Hayden, Y. Li, J.K. Cooper, C.A. Ross, S. Govoni, C. Vincenz, E. Cattaneo, Wild-type huntingtin protects from apoptosis upstream of caspase-3, J. Neurosci. 20 (2000) 3705–3713.
[31] L.W. Ho, R. Brown, M. Maxwell, A. Wyttenbach, D.C. Rubinsztein, Wild type huntingtin reduces the cellular toxicity of mutant huntingtin in mammalian cell models of Huntington's disease, J. Med. Genet. 38 (2001) 450–452.
[32] T.S. Tang, H. Tu, E.Y. Chan, A. Maximov, Z. Wang, C.L. Wellington, M.R. Hayden, I. Bezprozvanny, Huntingtin and huntingtin-associated protein 1 influence neuronal calcium signaling mediated by inositol-(1,4,5) triphosphate receptor type 1, Neuron 39 (2003) 227–239.
[33] M. Terasaki, L.B. Chen, K. Fujiwara, Microtubules and the endoplasmic reticulum are highly interdependent structures, J. Cell Biol. 103 (1986) 1557–1568.
[34] C. Lee, L.B. Chen, Dynamic behavior of endoplasmic reticulum in living cells, Cell 54 (1988) 37–46.

[35] G. Hoffner, P. Kahlem, P. Djian, Perinuclear localization of huntingtin as a consequence of its binding to microtubules through an interaction with beta-tubulin: relevance to Huntington's disease, J. Cell Sci. 115 (2002) 941–948.
[36] R. Burns, Rings, MAPs and microtubules, Nature 273 (1978) 709–710.
[37] J. Howard, A.A. Hyman, Dynamics and mechanics of the microtubule plus end, Nature 422 (2003) 753–758.
[38] N.S. Hachiya, K. Watanabe, Y. Sakasegawa, K. Kaneko, Microtubules-associated intracellular localization of the NH(2)-terminal cellular prion protein fragment, Biochem. Biophys. Res. Commun. 313 (2004) 818–823.
[39] N.S. Hachiya, K. Watanabe, M. Yamada, Y. Sakasegawa, K. Kaneko, Anterograde and retrograde intracellular trafficking of fluorescent cellular prion protein, Biochem. Biophys. Res. Commun. 315 (2004) 802–807.

0031-3998/05/5802-0263
PEDIATRIC RESEARCH
Vol. 58, No. 2, 2005
Printed in U.S.A.

Molecular Mechanism of a Temperature-Sensitive Phenotype in Peroxisomal Biogenesis Disorder

KAZUYUKI HASHIMOTO, ZENICHIRO KATO, TOMOKO NAGASE, NOBUYUKI SHIMOZAWA, KAZUO KUWATA, KENTARO OMOYA, AILIAN LI, EIJI MATSUKUMA, YUTAKA YAMAMOTO, HIDENORI OHNISHI, HIDEHITO TOCHIO, MASAHIRO SHIRAKAWA, YASUYUKI SUZUKI, RONALD J.A. WANDERS, AND NAOMI KONDO

Department of Pediatrics [K.H., Z.K., TN, N.S., K.O., AL, E.M., Y.Y., H.O., N.K.], Department of Biochemistry and Biophysics [K.K.], Medical Education Development Center [Y.S.], Gifu University School of Medicine, Gifu 501-1194, Japan, Graduate School of Integrated Science [H.T., M.S.], Yokohama City University, Yokohama 230-0045, Japan, Department of Clinical Chemistry and Pediatrics, Academic Medical Center, University of Amsterdam, 1100 DE Amsterdam, The Netherlands [R.J.A.W.]

ABSTRACT

Peroxisomal biogenesis disorders include Zellweger syndrome and milder phenotypes, such as neonatal adrenoleukodystrophy (NALD). Our previous study of a NALD patient with a marked deterioration by a fever revealed a mutation (Ile326Thr) within a SH3 domain of PEX13 protein (Pex13p), showing a temperature-sensitive (TS) phenotype in peroxisomal biogenesis. Clinical TS phenotypes also have been reported in several genetic diseases, but the molecular mechanisms still remain to be clarified. The immunofluorescent staining with anti-Pex13p antibody also revealed TS phenotype of the I326T mutant protein itself in the patient cells. Protease digestion of the recombinant Pex13p-SH3 domain showed an increase of protease susceptibility, suggesting a problem of mutant protein fold. Conformational analyses against urea denaturation using urea gradient gel electrophoresis or fluorescence emission from tryptophan residue revealed that the mutant protein should be easily unfolded. Far-UV circular dichroism (CD) spectra demonstrated that both wild-type and the mutant protein have antiparallel beta-sheets as their secondary structure with slightly different extent. The thermal unfolding profiles measured by CD showed a marked lower melting temperature for I326T protein compared with that of wild-type protein. Analysis of the protein 3D-structure indicated that the Ile326 should be a core residue for folding kinetics and the substitution of Ile326 by threonine should directly alter the kinetic equilibrium, suggesting a marked increase of the unfolded molecules when the patient had a high fever. Structural analyses of the protein in the other genetic diseases could provide an avenue for better understanding of genotype-phenotype correlations. **(*Pediatr Res* 58: 263–269, 2005)**

Abbreviations

AOX, peroxisomal acyl-CoA oxidase
CD, circular dichroism
DBP, D-bifunctional protein
GST, glutathione-S-transferase
NALD, neonatal adrenoleukodystrophy
PBD, peroxisomal biogenesis disorder
Pex, Peroxin
SH3, src-homology 3
TS, temperature-sensitive
TUG, transverse urea gradient
ZS, Zellweger syndrome

Peroxisomal disorders represent an expanding group of genetic disorders in humans and comprise ~20 different disorders (1,2). Generally, peroxisomal disorders are divided into two groups; PBD (MIM#601539) and single peroxisomal enzyme deficiencies. PBD include ZS (MIM#214100), NALD (MIM#202370), infantile Refsum disease (MIM#266510), and rhizomelic chondrodysplasia punctata type 1 (MIM#215100). Our recent studies have shown that there is genetic heterogeneity among these patients, as concluded from complementation studies that have so far shown 13 different groups (3). The exact functional role of these different PEX gene products (peroxins) is largely unknown, but recent studies have revealed part of the importing mechanisms of peroxisomal proteins in association with peroxisome targeting signal receptors 1 and 2 (4).

A central role in the peroxisomal assembly is played by the PEX13 protein (Pex13p) together with Pex14p and Pex5p (5). Pex13p is a peroxisomal membrane protein containing an SH3,

Received August 9, 2004; accepted December 7, 2004.
Correspondence: Zenichiro Kato, M.D., Ph.D., Department of Pediatrics, Gifu University School of Medicine, Yanagido 1-1, Gifu 501-1194, Japan; e-mail: zen-k@cc.gifu-u.ac.jp
Supported, in part, by a grant-in-aid for Scientific Research (13670791) from the Japan Society for the Promotion of Science, by a grant for Child Health and Development (14C-3) from the Ministry of Health, Labour and Welfare, by the Uehara Memorial Foundation, and by the Naito Foundation.

DOI: 10.1203/01.PDR.0000169984.89199.69

which typically requires the PxxP motif for its binding partners, as observed in Pex14p (6,7). Mutation analysis of PEX13 revealed that two patients belonging to complementation group H with the ZS and NALD phenotypes carried a nonsense and a missense mutation, respectively (8). The patient with the milder form, NALD, had a missense mutation with substitution of isoleucine (Ile) 326 by threonine (Thr), I326T, within a SH3 domain, and showed normal development just before a sudden deterioration with a high fever due to a respiratory infection. Additionally, the patient's fibroblasts showed a TS phenotype in peroxisome assembly and function (8).

TS phenotypes in human have been reported in several diseases, including anemia, thromboembolism, PBD, and trichothiodystrophy (8–11). The genotypes of the patients have been revealed, but the precise molecular mechanisms between genotypes and clinical phenotypes are still to be clarified. We report here a part of structural basis of the TS phenotype caused by the PEX13 mutation.

PATIENTS AND METHODS

Patient. The index patient is a male of Caucasian parents with a nonconsanguineous marriage. Pregnancy, delivery, and developmental milestones during the first postnatal year were normal. At age 16 mo he became ill with a high fever due to an upper respiratory infection, followed by rapidly progressive hypotonia and muscle weakness leading to severe generalized paresis that made gavage feeding necessary. Loss of hearing and visual decline followed within 6 mo of onset. No external dysmorphia or hepatosplenomegaly was observed.

Skin fibroblasts of the patient showed no catalase-containing particle, and the clinical features and the cytologic appearance of the fibroblasts were compatible to the phenotypes of neonatal adrenoleukodystrophy. Biochemical analyses including fatty acids indicated peroxisomal abnormalities (C24:0/C16:0: 0.15; normal control: 0.58), but dihydroxyacetone phosphate acyltransferase activity was normal in the patient's fibroblasts (patient: 2.26; control: 1.55 nmol/mg/120 min) (8).

The patient was classified as new group H, with the genetic mutation being the homozygote of T997C of the PEX13 gene resulting in a missense mutation, I326T (8). The cell lines obtained from the patient showed a TS phenotype in the peroxisomal biogenesis detected by catalase import after incubation at 30°C instead of 37°C. It was demonstrated in a gene expression experiment using the PEX13-defective CHO mutant that the I326T was indeed the TS mutation (8). This study was approved by the Institutional Review Board of Gifu University. Informed consent was obtained from parents.

Cell lines and immunofluorescence study. Fibroblasts from patient H02, who showed Zellweger phenotype (W234ter in PEX13), and patient K01, who showed Zellweger phenotype (Q189ter in PEX14), were used as negative controls in immunofluorescent staining. Fibroblasts from patient H01 (I326T in PEX13), patient H02 (W234ter in PEX13), patient K01 (Q189ter in PEX14), and control were cultured at 37°C or 30°C for 7 d (3,8). The cells were fixed with 4% paraformaldehyde/0.1 M potassium phosphate, pH 7.4, permeabilized with 0.1% Triton X-100/PBS, and blocked with 4% FCS/0.1% Triton X-100/PBS. In these fixed fibroblasts, peroxisomes were immunohistochemically stained with rabbit anti-rat-peroxisomal AOX and rabbit anti-human DBP antibodies. For double immunofluorescence staining, rabbit anti-rat Pex14p and mouse anti-human Pex13p (Abcam Ltd., Cambridge, UK) antibodies, and FITC-conjugated goat anti-rabbit (Tago Biosource International, Camarillo, CA) and Cy3-conjugated goat anti-mouse (Chemicon International, Temecula, CA) secondary antibodies were used. For observation we used a confocal laser-scanning microscope (LSMS PASCAL, Carl Zeiss GmbH, Jena, Germany) (12).

Purification of recombinant proteins. Protein expression and purification were performed as described previously with minor modification (13). Briefly, *Escherichia coli* BL21 cells were transformed with the vector, pGEX6P-3 coding the GST-fused *Homo sapiens* (Hs) Pex13p-SH3 domain, which was confirmed as a binding domain for Pex14p (14). The colony with the highest expression level was cultivated overnight in 200 mL of the LB medium with 100 μg/mL ampicillin. The culture was transferred into 2 L of the LB medium with 100 μg/mL ampicillin and incubated at 37°C until OD 600 = 0.45, and then was cooled to 18°C. IPTG (final concentration 0.1 mM) was added to the medium when OD 600 = 0.5. The culture was further incubated at 18°C for 7 h.

The bacterial cell pellet was resuspended in buffer-A (50 mM Tris-HCl, pH 8.0, 400 mM KCl, 10 mM 2-mercaptoethanol, and 1 mM EDTA) with 1 mM PefaBloc (Roche Molecular Biochemicals, Indianapolis, IN), lysed by sonication, and then centrifuged. The clear lysate was applied onto a GST affinity column (Amersham Pharmacia Biotech, Piscataway, NJ) and the column washed with buffer-A. The captured fusion protein was cleaved by PreScission protease (Amersham Pharmacia Biotech) at a ratio of 1% (wt/wt) at 4°C and HsPex13p-SH3(wild-type or I326T) protein was eluted by buffer-A.

Protease susceptibility assay. Twenty microliters of GST-Pex13p(wild-type) or (I326T) (1 mg/mL) was incubated with 0.1% wt/wt of chymotrypsin at 20, 30, or 40°C for 1 h and analyzed by SDS-PAGE (15–25% gradient).

Conformational stability analyses of HsPex13-SH3. Conformational stability of HsPex13-SH3(wild-type or I326T) was analyzed by TUG gel electrophoresis and fluorometry (10,15). TUG polyacrylamide gels [linear gradient 0–8 M urea in 7.5% (wt/vol) acrylamide] were prepared as previously described with minor modification using the DCode system (Bio-Rad, Hercules, CA) (10). Tris-glycine buffer (25 mM Tris,192 mM glycine) was used as a running buffer. One hundred micrograms of HsPex13-SH3(wild-type or I326T) was dissolved in sample buffer (62.5 mM Tris-HCl pH6.8, 40% glycerol, 0.01% BPB) and applied evenly across the top of the gel, and electrophoresis was performed at 25 mA constant current for 3 h, keeping the buffer and the gel at 20°C with the DCode temperature control system.

Conformational stability of HsPex13-SH3(wild-type or I326T) was also analyzed as previously described with minor modification using a F-2000 fluorimeter (Hitachi, Yokohama, Japan) (15). Tryptophan residues were selectively excited at 295 nm and the emitted signal was recorded from 309 to 550 nm. Measurements were performed at 20°C in 50 mM phosphate buffer (pH 7.5) containing 100 mM Na_2SO_4. Urea (1–8 M) was used as the denaturant and the protein concentration in each experiment was 15 μM.

Circular dichroism of HsPex13-SH3 at different temperatures. All the circular dichroism (CD) measurements were acquired using an Aviv 202 stopped-flow circular dichroism spectrometer (Aviv Associated, Lakewood, NJ) (16,17). Far-UV CD spectra were recorded between 200 and 250 nm, using a 1-nm slit width and a 0.1-cm path length cell thermostated at 5°C. Typically, CD signals were collected for 10 s at each wavelength. Thermal unfolding of HsPex13-SH3 was monitored by measuring the CD signal at 218 nm containing 62 μM of HsPex13-SH3 in 50 mM phosphate buffer (pH 7.5) with 100 mM Na_2SO_4 in a temperature range from 5 to 85°C with a heating rate of 1°C/min.

Sequence alignment and homology modeling of the structures. The sequence alignment of the Pex13p-SH3 domains of different species and the HsFyn-SH3 domain were performed by ClustalW with a BLOSUM matrix (18). Homology modeling of the HsPex13-SH3 domain was performed with a Geno3D system using the crystal structure of the *Saccharomyces cerevisiae* (Sc) Pex13-SH3 domain (PDB code: 1N5Z) as a template (19). Structural verification of the calculated models was performed with PROCHECK (20). Structural rendering was performed with RasMol software (21).

RESULTS

Immunofluorescence studies of patient fibroblasts. Fibroblasts of the control, patients H01 (I326T), H02 (W234ter), and K01 (Q189ter in PEX14) were incubated for 7 d at 37°C or 30°C and subjected to immunofluorescence staining. The punctuate staining pattern for intact peroxisomes and the intact import of AOX and DBP were observed in the control fibroblasts at 37°C and 30°C (Fig. 1), whereas no immunofluorescence stained particles with these antibodies could be observed in the H02 fibroblasts at either 37°C or 30°C (Fig. 1). In the H01 fibroblasts, only a few particles could be observed at 37°C (Fig. 1, *A-a* and *B-a*), whereas numerous particles could be observed at 30°C (Figure 1, *A-d* and *B-d*), indicating a TS phenotype.

In a double immunofluorescence staining study using mouse anti-Pex13p and rabbit anti-Pex14p antibodies, expression of Pex13p on peroxisomes was also impaired at 37°C in H01 cells (Fig. 2*A-e*); but it was restored at 30°C (Fig. 2*B-e*), indicating the temperature-sensitive nature of the protein with the I326T mutation. In addition, the Pex14p assembly on the peroxisomes

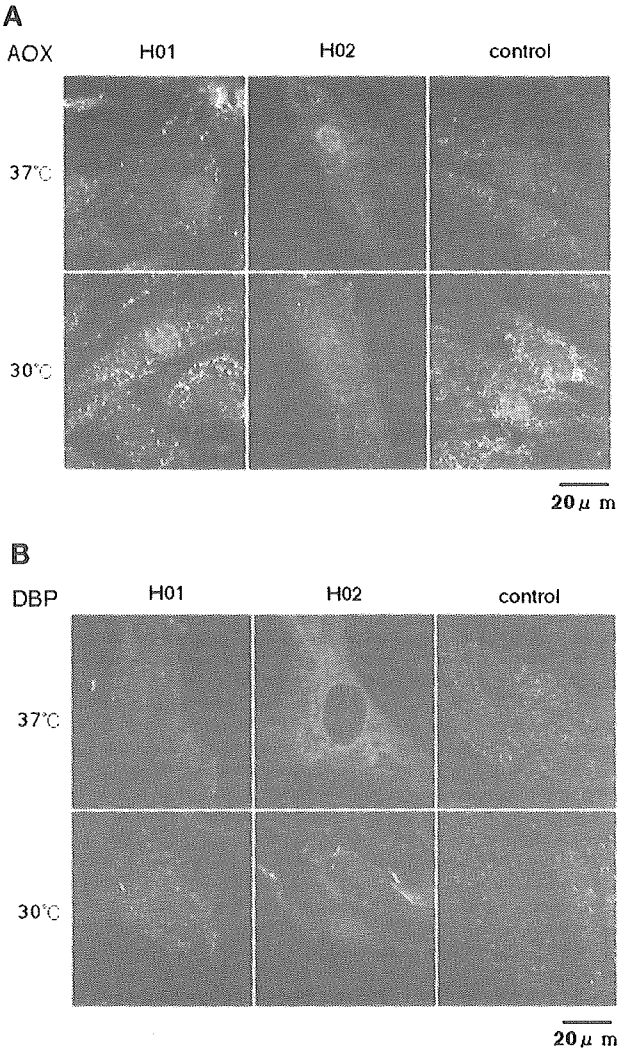

Figure 1. Protein import into peroxisomes depends on temperature in fibroblasts harboring the mutation I326T in PEX13. Fibroblasts from control, patient H01 (I326T in PEX13), and patient H02 (W234ter in PEX13) were cultured at 37°C or 30°C. Cells were stained with (*A*) anti-human AOX and (*B*) anti-human DBP rabbit antibodies, and anti-rabbit IgG antibody with FITC. Import of peroxisomal enzymes is impaired at 37°C in H01 cells, but is restored at 30°C, indicating the temperature-sensitive phenotype of peroxisomal biogenesis with protein import *via* peroxisomal targeting signal receptors. In contrast, H02 cells show no restoration, even at 30°C.

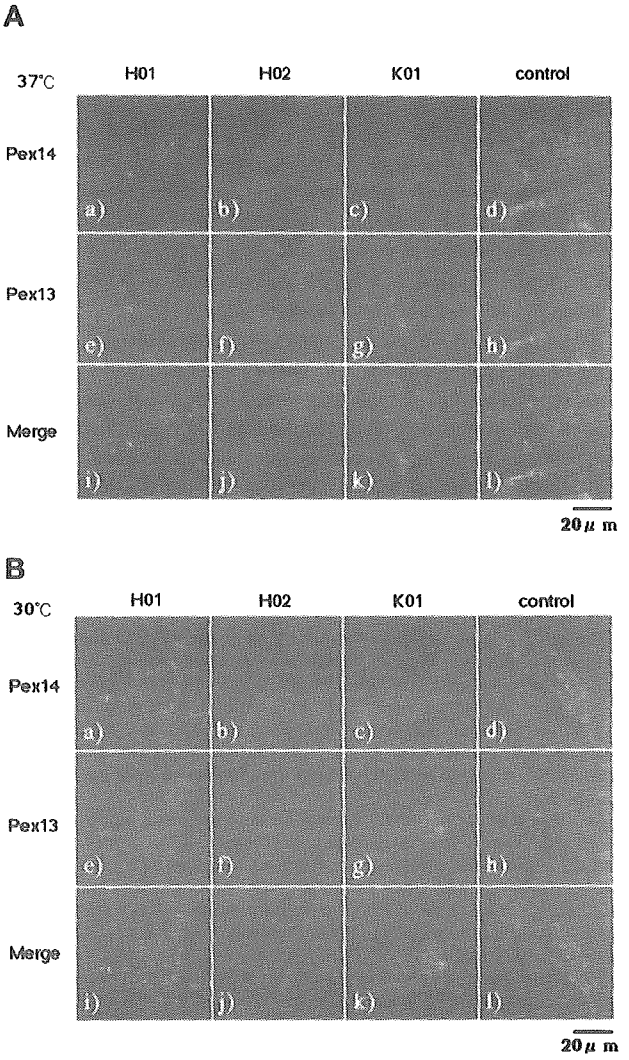

Figure 2. Pex13p expression and Pex14p assembly depend on temperature in fibroblasts harboring the mutation I326T in PEX13. Fibroblasts from control, patient H01 (I326T in PEX13), patient H02 (W234ter in PEX13), and patient K01 (Q189ter in PEX14) were cultured at (*A*) 37°C or (*B*) 30°C for 7 d. Cells were stained with mouse anti-human Pex13 and rabbit anti-rat Pex14p antibodies. Expression of Pex13p on peroxisomes is impaired at 37°C in H01 cells, but it is restored at 30°C, indicating the temperature-sensitive nature of protein with the I326T mutation. Pex14p assembly on the peroxisomes is also impaired at 37°C in H01 cells, but is restored at 30°C, suggesting that the loss of assembly of HsPex14p in H01 cells is due to the lack of the HsPex13p adaptor function.

was also impaired at 37°C in H01 cells (Fig. 2*A-a*), so that the assembly of Pex14p on peroxisomes was dependent on Pex13p expression, but not *vice versa*. Neither Pex13p nor Pex14p expression was detected in the H02 fibroblasts at 37°C or 30°C (Fig. 2). However, an amount of Pex14p equivalent to that of wild-type cells was confirmed in the H01 and H02 cell lysates by immunoblot analysis (authors' unpublished data). The findings suggested that Pex14p incorporation into the *peroxisome* in H01 cells was not due to its defect, but that the impairment was due to the lack of the HsPex13p binding function (22).

Protease susceptibility assay. Protease susceptibility of Pex13p was examined with chymotrypsin. HsPex13p-SH3(I326T) incubated with chymotrypsin showed marked susceptibility to protease cleavage at all temperatures compared with HsPex13p-SH3(wild-type) (Fig. 3). The finding suggested that the problem of SH3 domain fold in I326T mutant, which results in an increase of protease susceptibility.

Conformational stability analyses of HsPex13-SH3. TUG gel analysis of HsPex13p-SH3 protein showed a significant migration between HsPex13-SH3(*wild-type*) and HsPex13-SH3(I326T), both showing a sigmoidal transition curve (Fig. 4*A*). Co-electrophoresis of mixed sample of HsPex13-SH3(wild-type) and HsPex13-SH3(I326T) clearly showed the difference of migration between them (Fig. 4*B*). HsPex13-

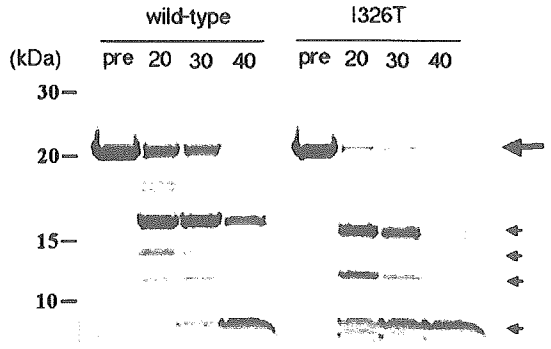

Figure 3. Protease susceptibility of Pex13p(I326T). HsPex13p-SH3(wild-type or I326T) was incubated with 0.1% wt/wt of chymotrypsin at 20, 30, or 40°C for 1 h and analyzed by SDS-PAGE. HsPex13p-SH3(I326T) incubated with chymotrypsin shows marked susceptibility against protease cleavage at all temperatures compared with HsPex13p-SH3(wild-type). These findings indicate that the protein structure of HsPex13p-SH3(I326T) itself also has a temperature-sensitive character. *Large arrow,* intact Pex13p-SH3; *small arrows,* cleaved fragments; *pre,* preincubation; *20,30,40,* incubation temperature.

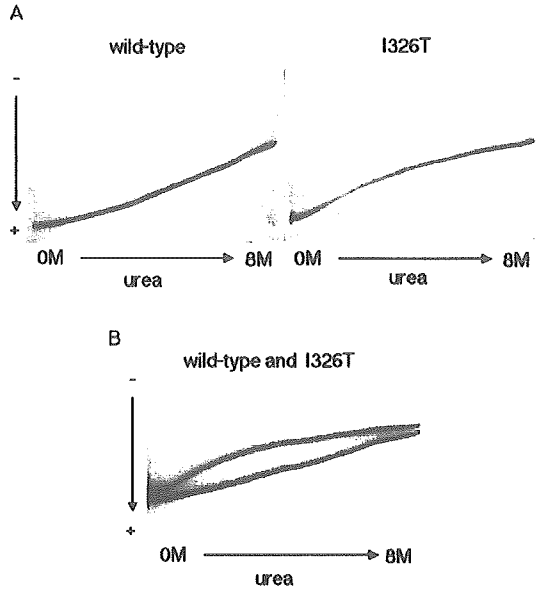

Figure 4. TUG gel analysis of HsPex13p-SH3 protein. (*A*) Electrophoresis of (*left*) HsPex13-SH3(wild-type) or (*right*) HsPex13-SH3(I326T) was performed on TUG polyacrylamide gels [linear gradient 0–8 M urea in 7.5% (wt/vol) acrylamide] using the DCode system (Bio-Rad), keeping the temperature at 20°C. Migration of HsPex13-SH3(I326T) showed a significantly different pattern compared with that of HsPex13-SH3(wild-type), having a sigmoidal curve. (*B*) Co-electrophoresis of mixed sample of HsPex13-SH3(wild-type) and HsPex13-SH3(I326T). Co-electrophoresis clearly showed the difference of migration between HsPex13-SH3(wild-type) and HsPex13-SH3(I326T). HsPex13-SH3(I326T) migrated similar to the HsPex13-SH3(wild-type) at 0 M or 8 M urea region, suggesting similar native or denatured conformations of them. However, the half point of the conformational transition in HsPex13-SH3(I326T) was observed at around 2 M, whereas that in HsPex13-SH3(wild-type) was observed at around 4 M. These results indicate that the conformational stability of HsPex13-SH3(I326T) is markedly lower than that of HsPex13-SH3(wild-type).

SH3(I326T) migrated similarly to the HsPex13-SH3(wild-type) at around the 0 M and 8 M urea region, suggesting similar native and denatured conformations. However, the half point of the conformational transition in HsPex13-SH3(I326T) was observed at 2 M, whereas that in HsPex13-SH3(wild-type) was observed at 4 M. These results indicate that the conformational stability of HsPex13-SH3(I326T) is markedly lower than that of HsPex13-SH3(wild-type).

Conformational changes of HsPex13-SH3(wild-type or I326T) were examined using fluorescence from tryptophan (excitation, 295; and emission, above 309 nm). Fluorescence spectra were obtained in the same buffer with or without 8 M urea at 20°C (Fig. 5*A*). HsPex13-SH3(wild-type or I326T) in the absence of urea showed a different peak emission wavelength (wild-type, 336 nm; I326T, 342 nm) and intensity, whereas those in the presence of 8 M urea showed the same peak emission wavelength with a significant red-shift at 350 nm and the same intensity, which were significantly higher than those of protein without urea. These results indicate that the peak wavelength and intensity increases with the degree of exposure of the tryptophan residue in the SH3 domain (residue number Trp313 of HsPex13) to the solvent.

Transitions of the peak wavelength were monitored with a different urea concentration (0–8 M). HsPex13-SH3(wild-type) showed a sigmoidal transition of the peak emission wavelength changing from 336 to 350 nm, whereas HsPex13-SH3(I326T) showed a lesser sigmoidal transition of the peak changing from 342 to 350 nm (Fig. 5*B*). These findings indicate that HsPex13-SH3(I326T) has a different population of native conformation even in a native condition at 20°C.

Circular dichroism of PEX13-SH3 at different temperatures. Far-UV CD spectra at 5°C in Figure 6*A* demonstrates that both HsPex13-SH3(wild-type) and HsPex13-SH3(I326T) have a minima around 218 nm, which corresponds to the

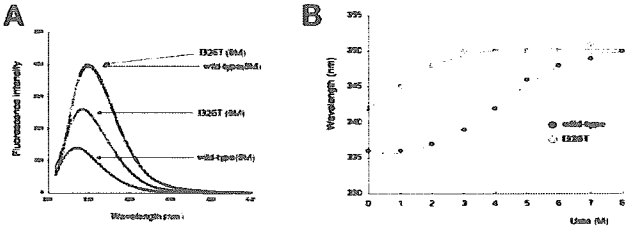

Figure 5. Conformational changes in denaturation by urea. (*A*) Conformational changes of HsPex13-SH3(wild-type or I326T) was measured using fluorescence from tryptophan (excitation, 295; and emission, above 309 nm). Measurements were performed at 20°C in 50 mM phosphate buffer (pH 7.5) containing 100 mM Na_2SO_4 with or without 8 M urea. HsPex13-SH3(wild-type or I326T) in the absence of urea showed a different emission peak and intensity (wild-type, 336 nm; I326T, 342 nm), whereas in the presence of 8 M urea showed the same emission peak at 350 nm and the same intensity significantly higher than those of protein in native state. These results indicate that the peak wavelength and intensity will increase with the degree of exposure of the tryptophan residue in the SH3 domain (residue number Trp313) and the native state protein of HsPex13-SH3(I326T) should have a different tertiary structure around Trp313. (*B*) Monitoring of the peak wavelength in emissions with a different urea concentration (0–8 M). HsPex13-SH3(wild-type) showed a lesser sigmoidal transition of the peak changing from 336 to 350 nm, whereas HsPex13-SH3(I326T) showed a nonsigmoidal transition of the peak changing from 342 to 350 nm. These findings indicate that HsPex13-SH3(I326T) has a structure with more exposed Trp313 even at native condition, and the population of the mutant protein would be skewed for the unfolded state even at 20°C.

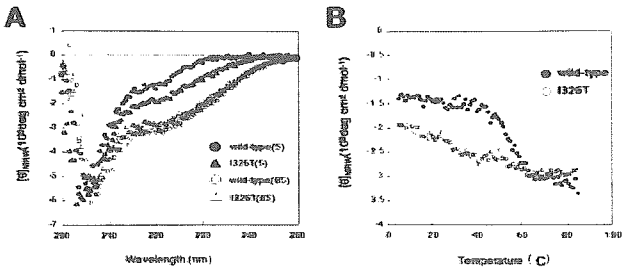

Figure 6. CD spectra of Pex13p-SH3. (*A*) CD spectra of Pex13p-SH3 in native and denatured states. The values of wild-type and I326T protein at 5°C have a similar minima at around 218 nm, which corresponds to the typical anti-parallel beta-sheets, but with different intensities. On the other hand, thermally unfolded CD spectra at 85°C are almost the same for both proteins, suggesting similar unfolded conformations. The measured temperatures are indicated in parenthesis. (*B*) Transition of HsPex13p-SH3(I326T) at a lower temperature. Melting temperature (Tm) of HsPex13-SH3 (wild-type) is ~58°C. However, Tm of HsPex13-SH3 (I326T) is significantly low, *i.e.* around 30°C. The significantly low thermal stability of HsPex13-SH3 (I326T) results in a low population of the native conformation even at 30°C. When the temperature increases over 40°C, most of the population may lose their native folds.

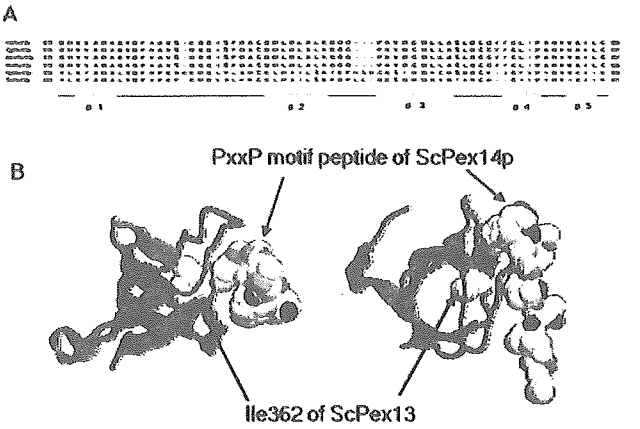

Figure 7. Structural analyses of Pex13p-SH3. (*A*) Sequence alignment of the Pex13-SH3 domains among different species (Hs: *Homo sapiens*, Mm: *Mus musculus*, Rn: *Rattus norvegicus*, Cg: *Cricetulus griseus*, Pp: *Pichia pastoris*, Sc: *Saccharomyces cerevisiae*), showing striking similarities, especially in mammalian species (>95%). Amino acid identities among yeasts and mammalians are relatively lower (about 30%), but the substitutions are mostly conservative. Isoleucine at 326 of HsPex13p is well conserved, except for PpPex13p but has a conservative amino acid, valine. (*B*) Crystal structure of ScPex13p. Ile362 of ScPex13p, corresponding to Ile326 of HsPex13, is one of the hydrophobic core residues of the beta-barrel structure of the SH3 domain, and the residue also consists of a recognition site for the PxxP motif of ScPex14p, suggesting that the substitution of the residue affects the structure and the binding activity. The overall structures are shown as a ribbon model and the residues of Ile362 of ScPex13p and the peptide with the PxxP motif of ScPex14p are indicated in spacefill representations—carbon in *gray*, nitrogen in *blue*, and oxygen in *red*.

typical antiparallel beta-sheets, but with different intensities. Antiparallel beta sheets are characteristic to the SH3 domain structures (17). On the other hand, thermally unfolded CD spectra at 85°C are almost the same for both proteins, suggesting similar unfolded conformations (Fig. 6*A*). A decrease of intensities at 218 nm upon unfolding may be due to an increase of the intermolecular interaction (intermolecular beta-sheet formation) and/or the change of contribution from the aromatic side-chain absorption. However, to address the differences in thermal stability between the two proteins, we measured their thermal denaturation profiles.

Thermal unfolding profiles for both proteins measured by CD intensities at 218 nm is displayed in Fig. 6*B*. Melting temperature (Tm) of HsPex13-SH3(wild-type) is ~58°C. However, melting temperature of HsPex13-SH3(I326T) is significantly lower, *i.e.* around 30°C. The significantly low thermal stability of HsPex13-SH3(I326T) results in a low population of the native conformation even at 30°C. When the temperature increases over 40°C, most of the population may lose their native folds (Fig. 6*B*). Thermal denaturation processes of HsPex13-SH3(wild-type) and HsPex13-SH3(I326T) were fully reversible between 5 and 85°C (data not shown).

Sequence alignment and homology modeling of the structures. The sequence alignment of the Pex13p-SH3 domains of different species showed striking similarities, especially in mammalian species (>95%) (Fig. 7*A*). The amino acid identities among yeasts and mammalians were not so high (about 30%), but the substitutions of the amino acids were mostly conservative. Ile at 326 of HsPex13p is well conserved, except for *Pichia pastoris* Pex13p, but has a conservative amino acid, valine (Fig. 7*A*). The crystal structure showed that the Ile362 of ScPex13p, which corresponds to Ile326 of HsPex13, is one of the hydrophobic core residues of the beta-barrel structure of the SH3 domain, and that the residue also consists of a recognition site for the PxxP motif of ScPex14p, suggesting that the substitution of the residue affects structure and binding activity (Fig. 7*B*).

Alignment of the HsPex13-SH3 and HsFyn-SH3 domains showed high similarity, and that the core "nucleus" hydrophobic residues, Ile28, Ala39, and Ile50, of HsFyn-SH3 determined by protein folding kinetic analyses (15,17) were also conserved in HsPex13-SH3 (Fig. 8*A*). Homology modeling of the HsPex13-SH3 domain confirmed that these three core nuclei residues were also structurally conserved (Fig. 8*B*, left and center).

However, the mutant SH3 domain with I326T has a different main chain topology, especially around the interface for peptide binding. Moreover, the core nucleus residues could be only loosely formed due to the negatively charged side chain of Thr (Fig. 8*B*, right). These findings suggest that the overall structure of the SH3(I326T) mutant would be fragile and be susceptible to protease digestion, which results in loss of interaction between SH3(I326T) and Pex14p.

DISCUSSION

Pex13p has a central role in the assembly of peroxisomal proteins, and interaction with Pex14p is a critical step for peroxisomal biogenesis (5,8). Pex13p has an SH3 domain in the C-terminal region that is known as an adaptor domain for the PxxP motif peptide, one that Pex14p also has (6,7). Our observations of the patient's fibroblasts revealed the temperature-sensitive nature of biogenesis of peroxisomes and import

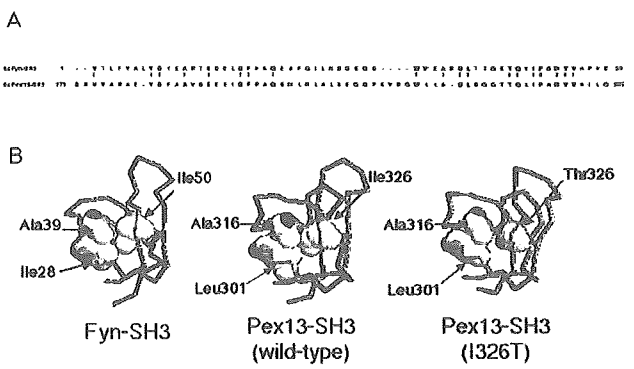

Figure 8. Conservation of hydrophobic core residues in Pex13p-SH3. (*A*) Alignment of the HsPex13-SH3 and HsFyn-SH3 domains. The HsFyn-SH3 domain is numbered according to Northey *et al.* (15) The high similarity indicates that conservation of the core "nucleus" hydrophobic residues, Ile28, Ala39, and Ile50, of HsFyn-SH3 is important for protein folding. (*B*) Structural comparison between HsFyn-SH3 and HsPex13-SH3s. Homology modeling of the HsPex13-SH3 domain confirms the structural conservation of the core "nucleus" hydrophobic residues. However, the mutant SH3 domain with I326T shows a different main chain topology especially around the interface for peptide binding, and the core nucleus residues can be only loosely formed due to the negatively charged side chain of Thr. The overall structures are shown as the main chain backbone, and the critical nucleus residues are indicated as spacefill representations, as in Figure 7.

of peroxisomal enzymes (Fig. 1) (8). In addition, assembly of Pex14p also showed a temperature-sensitive character that depended on Pex13p expression (Fig. 2). The temperature-sensitive nature of the expression of HsPex13p(I326T) on peroxisomes suggests that the produced protein, especially the SH3 domain, is fragile and was degraded at 37°C, but that the protein structure could be maintained preserving its binding activity with Pex14p at 30°C (Fig. 2).

The principal stabilizing element in globular proteins such as the SH3 domain is the hydrophobic core, a subset of hydrophobic residues that is shielded from solvents in the native state structure. The role of hydrophobic core residues in maintaining the thermodynamic stability of proteins has been demonstrated; and protein folding kinetics studies have indicated a key role for hydrophobic core residues not only in stabilizing the native state but also in driving the folding reaction itself (15). Compaction of the hydrophobic core occurs in the early stages of folding and resulted in significant reductions in the folding rate caused by substitutions at a distinct region of the hydrophobic core (23,24).

In the HsFyn-SH3 domain, the stability and folding kinetics of protein have been characterized using >40 mutant proteins (15). The results showed that three core nucleus residues, Ile28, Ala39, and Ile 50 (Fig. 8*B*, left), were tightly packed even in the transition state of folding, and that substitutions at these positions cause the largest changes in the stability in the native state, and also in the folding rate; for example, the alanine mutant of Ile50 showed significant reduction in Tm (wild-type: 80.1°C; I50A: 44.2°C). Introducing the mutation also altered the folding and the unfolding kinetics at 25°C (folding *versus* unfolding: wild-type, 30.2/s *versus* 0.51/s; I50A, 4.2/s *versus* 13.8/s), indicating that slower folding and faster unfolding resulted in an equilibrium with the larger unfolded population of the proteins even at a temperature lower than its melting temperature (15). Similar characteristics of core nucleus residues have been investigated in other SH3 domains showing similar results (17,23–25).

Ile326 of HsPex13p-SH3 is a hydrophobic core residue of the barrel structure of the domain and also should act as a key core nucleus residue for protein folding with Leu301 and Ala316 (Fig. 8*B*, center). The substitution of Ile50 by serine of HsFyn-SH3 showed a drastic reduction in peptide binding activity with marked protein instability, suggesting similar effects as by the I326T mutation, introducing a charged side chain of threonine into the hydrophobic core of HsPex13p-SH3 (Fig. 8*B*, right). Protein stability assays performed here have shown the fragility of the SH3 domain conformation (Figs. 3–5), and that the melting temperature of I326T estimated by CD was markedly lower than 37°C (Tm: wild-type, 58°C; I326T, 30°C). These findings indicate that a large population of the expressed protein is not correctly folded even at a normal body temperature (Fig. 6*B*). The temperature-sensitive nature of the mutation I326T in HsPex13p should be recognized, not only as simple fragility, such as susceptibility to the proteases of the native protein, but also as an imbalance of folding and unfolding kinetics, which results in an increase of unfolded proteins even at a lower temperature, something similarly observed in other SH3 mutants (15,24,25).

From the findings above, it can be assumed that when a patient with the I326T mutation in Pex13p has a high body temperature, such as 40°C, correctly folded protein would be almost lost, and the loss of Pex13p leads to the loss of assembly of the peroxisomal targeting receptors including Pex14p; then total peroxisomal biogenesis would be abolished, with the dysfunction leading to the deterioration of the patient. Moreover, a large proportion of Pex13p is unfolded even at a normal body temperature, but the residual adaptor activity by correctly folded proteins can somehow maintain peroxisomal functions as shown in the residual activity of the fatty acid metabolism (4,8). In PBD, TS phenotypes in Pex1, Pex2, and Pex6 with milder forms have been reported (26,27) and therapeutic effects have been reported in cells from patients with milder phenotypes, but not those with the severe phenotype, ZS (28). Treatment of PBD fibroblasts with 4-phenylbutyrate showed an induction of peroxisomes having a 2-fold increase in transcription of related genes. If the absolute amount of correctly folded protein increases even with the same ratio of the unfolded protein, it could provide a protective treatment for TS phenotype patients.

Mutation effects of noncatalytic residues in genetic diseases have been implicated simply as protein degradation by structural instability. However, as shown in this study, which has directly revealed the folding state of protein in the TS phenotype mutation (I326T), more precise investigations utilizing structural analyses could reveal the true nature of the mutations; showing a part of pathogenesis of TS phenotype in peroxisomal disease. The structural approaches in the other genetic diseases also can contribute to better understanding of genotype-phenotype correlation and assist the development of new therapeutic approaches including the use of chemical chaperones (29).

Acknowledgments. The authors thank M. Komori for providing anti-Pex13p antibody and N. Usuda for anti-AOX and DBP antibodies. We also thank Y. Yatsuda, A. Seki, S. Shimizu, Y. Kondo, M. Kojima, and K. Kasahara for their assistance.

REFERENCES

1. Moser HW 1999 Genotype-phenotype correlations in disorders of peroxisome biogenesis. Mol Genet Metab 68:316–327
2. Fujiki Y 2000 Peroxisome biogenesis and peroxisome biogenesis disorders. FEBS Lett 476:42–46
3. Shimozawa N, Tsukamoto T, Nagase T, Takemoto Y, Koyama N, Suzuki Y, Komori M, Osumi T, Jeannette G, Wanders RJ, Kondo N 2004 Identification of a new complementation group of the peroxisome biogenesis disorders and PEX14 as the mutated gene. Hum Mutat 23:552–558
4. Suzuki Y, Shimozawa N, Orii T, Tsukamoto T, Osumi T, Fujiki Y, Kondo N 2001 Genetic and molecular bases of peroxisome biogenesis disorders. Genet Med 3:372–376
5. Urquhart AJ, Kennedy D, Gould SJ, Crane DI 2000 Interaction of Pex5p, the type 1 peroxisome targeting signal receptor, with the peroxisomal membrane proteins Pex14p and Pex13p. J Biol Chem 275:4127–4136
6. Douangamath A, Filipp FV, Klein AT, Barnett P, Zou P, Voorn-Brouwer T, Vega MC, Mayans OM, Sattler M, Distel B, Wilmanns M 2002 Topography for independent binding of α-helical ligands to a peroxisomal SH3 domain. Mol Cell 10:1007–1017
7. Kami K, Takeya R, Sumimoto H, Kohda D 2002 Diverse recognition of non-PxxP peptide ligands by the SH3 domains from p67(phox), Grb2 and Pex13p. EMBO J 21:4268–4276
8. Shimozawa N, Suzuki Y, Zhang Z, Imamura A, Toyama R, Mukai S, Fujiki Y, Tsukamoto T, Osumi T, Orii T, Wanders RJ, Kondo N 1999 Nonsense and temperature-sensitive mutations in PEX13 are the cause of complementation group H of peroxisome biogenesis disorders. Hum Mol Genet 8:1077–1083
9. Zinkham WH, Liljestrand JD, Dixon SM, Hutchison JL 1979 Observations on the rate and mechanism of hemolysis in individuals with Hb Zurich [His E7(63) leads to Arg]: II. Thermal denaturation of hemoglobin as a cause of anemia during fever. Johns Hopkins Med J 144:109–116
10. Bruce D, Perry DJ, Borg JY, Carrell RW, Wardell MR 1994 Thromboembolic disease due to thermolabile conformational changes of antithrombin Rouen-VI (187 Asn-Asp). J Clin Invest 94:2265–2274
11. Vermeulen W, Rademakers S, Jaspers NG, Appeldoorn E, Raams A, Klein B, Kleijer WJ, Hansen LK, Hoeijmakers JH 2001 A temperature-sensitive disorder in basal transcription and DNA repair in humans. Nat Genet 27:299–303
12. Shimozawa N, Tsukamoto T, Suzuki Y, Orii T, Shirayoshi Y, Mori T, Fujiki Y 1992 A human gene responsible for Zellweger syndrome that affects peroxisome assembly. Science 255:1132–1134
13. Li A, Kato Z, Ohnishi H, Hashimoto K, Matsukuma E, Omoya K, Yamamoto Y, Kondo N 2003 Optimized gene synthesis and high expression of human interleukin-18. Protein Expr Purif 32:110–118
14. Otera H, Setoguchi K, Hamasaki M, Kumashiro T, Shimizu N, Fujiki Y 2002 Peroxisomal targeting signal receptor Pex5p interacts with cargoes and import machinery components in a spatiotemporally differentiated manner: conserved Pex5p WXXXF/Y motifs are critical for matrix protein import. Mol Cell Biol 22:1639–1655
15. Northey JG, Di Nardo AA, Davidson AR 2002 Hydrophobic core packing in the SH3 domain folding transition state. Nat Struct Biol 9:126–130
16. Kuwata K, Matumoto T, Cheng H, Nagayama K, James TL, Roder H 2003 NMR-detected hydrogen exchange and molecular dynamics simulations provide structural insight into fibril formation of prion protein fragment 106–126. Proc Natl Acad Sci U S A 100:14790–14795
17. Mok YK, Elisseeva EL, Davidson AR, Forman-Kay JD 2001 Dramatic stabilization of an SH3 domain by a single substitution: roles of the folded and unfolded states. J Mol Biol 307:913–928
18. Rastogi PA 2000 MacVector. Integrated sequence analysis for the Macintosh. Methods Mol Biol 132:47–69
19. Combet C, Jambon M, Deleage G, Geourjon C 2002 Geno3D: automatic comparative molecular modelling of protein. Bioinformatics 18:213–214
20. Laskowski RA, Rullmannn JA, MacArthur MW, Kaptein R, Thornton JM 1996 AQUA and PROCHECK-NMR: programs for checking the quality of protein structures solved by NMR. J Biomol NMR 8:477–486
21. Sayle RA, Milner-White EJ 1995 RASMOL: biomolecular graphics for all. Trends Biochem Sci 20:374
22. Fransen M, Vastiau I, Brees C, Brys V, Mannaerts GP, Van Veldhoven PP 2004 Potential role for Pex19p in assembly of PTS-receptor docking complexes. J Biol Chem 279:12615–12624
23. Martinez JC, Serrano L 1999 The folding transition state between SH3 domains is conformationally restricted and evolutionarily conserved. Nat Struct Biol 6:1010–1016
24. Riddle DS, Grantcharova VP, Santiago JV, Alm E, Ruczinski I, Baker D 1999 Experiment and theory highlight role of native state topology in SH3 folding. Nat Struct Biol 6:1016–1024
25. Di Nardo AA, Larson SM, Davidson AR 2003 The relationship between conservation, thermodynamic stability, and function in the SH3 domain hydrophobic core. J Mol Biol 333:641–655
26. Imamura A, Shimozawa N, Suzuki Y, Zhang Z, Tsukamoto T, Fujiki Y, Orii T, Osumi T, Wanders RJ, Kondo N 2000 Temperature-sensitive mutation of PEX6 in peroxisome biogenesis disorders in complementation group C (CG-C): comparative study of PEX6 and PEX1. Pediatr Res 48:541–545
27. Walter C, Gootjes J, Mooijer PA, Portsteffen H, Klein C, Waterham HR, Barth PG, Epplen JT, Kunau WH, Wanders RJ, Dodt G 2001 Disorders of peroxisome biogenesis due to mutations in PEX1: phenotypes and PEX1 protein levels. Am J Hum Genet 69:35–48
28. Wei H, Kemp S, McGuinness MC, Moser AB, Smith KD 2000 Pharmacological induction of peroxisomes in peroxisome biogenesis disorders. Ann Neurol 47:286–296
29. Perlmutter DH 2002 Chemical chaperones: a pharmacological strategy for disorders of protein folding and trafficking. Pediatr Res 52:832–836

Neuroradiology (2005) 47: 501–506
DOI 10.1007/s00234-005-1372-x

Akio Soeda
Toshihiko Nakashima
Ayumi Okumura
Kazuo Kuwata
Jun Shinoda
Toru Iwama

Cognitive impairment after traumatic brain injury: a functional magnetic resonance imaging study using the Stroop task

Received: 15 October 2004
Accepted: 31 January 2005
Published online: 23 June 2005

A. Soeda (✉) · T. Iwama
Department of Neurosurgery,
Gifu University School of Medicine,
1-1 Yanagido, Gifu City 501-1194, Japan
E-mail: ccd29400@nyc.odn.ne.jp
Tel.: +81-58-2306271
Fax: +81-58-2306272

T. Nakashima · A. Okumura · J. Shinoda
Chubu Medical Center for Prolonged Traumatic Brain Dysfunction,
Department of Neurosurgery, Kizawa Memorial Hospital, Minokamo, Japan

K. Kuwata
Department of Biochemistry and Biophysics, Gifu University School of Medicine, Gifu, Japan

Abstract The anterior cingulate cortex (ACC) plays a key role in cognition, motor function, and emotion processing. However, little is known about how traumatic brain injury (TBI) affects the ACC system. Our purpose was to compare, by functional magnetic resonance imaging (fMRI) studies, the patterns of cortical activation in patients with cognitive impairment after TBI and those of normal subjects. Cortical activation maps of 11 right-handed healthy control subjects and five TBI patients with cognitive impairment were recorded in response to a Stroop task during a block-designed fMRI experiment. Statistical parametric mapping (SPM99) was used for individual subjects and group analysis. In TBI patients and controls, cortical activation, found in similar regions of the frontal, occipital, and parietal lobes, resembled patterns of activation documented in previous neuroimaging studies of the Stroop task in healthy controls. However, the TBI patients showed a relative decrease in ACC activity compared with the controls. Cognitive impairment in TBI patients seems to be associated with alterations in functional cerebral activity, especially less activation of the ACC. These changes are probably the result of destruction of neural networks after diffuse axonal injury and may reflect cortical disinhibition attributable to disconnection or compensation for an inefficient cognitive process.

Keywords Cognitive function · Functional MRI · Brain injury · Stroop task

Introduction

Follow-up studies of patients with traumatic brain injury (TBI) disclosed cognitive dysfunction even in patients with good neurological recovery [1–5]. In spite of advances in acute care and rehabilitation, these deficits interfere with the rehabilitation process, social re-integration, and the ability to function independently.

Several neuroimaging studies revealed structural, cerebral blood flow, and metabolic abnormalities following TBI [2, 3], such as corpus callosal atrophy [4] and anterior temporal dysfunction [5]. However, these studies assessed the patient at resting condition, a status in which neural activity is different from task-related neural activity. Positron-emission tomography (PET) or functional magnetic resonance imaging (fMRI) has been applied to assess changes in neural circuitry in response to specific tasks with well-described functional neuroanatomical characteristics [6]. For example, in an fMRI study of working memory, TBI patients showed increased activation of right frontal regions and generally increased dispersion of activation [7]. In a PET study, they manifested reduced frontal activation during free recall and increased frontal activation during recognition [8]. However, in those studies, working memory tasks that stress these networks were used, and

other cognitive functions, such as attention and emotional disorders, were not taken into consideration.

Psychological studies indicated that cognitive impairment was related to frontal and anterior cingulate cortex (ACC) abnormalities [9, 10], and fMRI studies provided information regarding the role of the ACC during the Stroop task [11–15]. This task is a classical experimental paradigm used in cognitive neuroscience to probe attention phenomena [16]. These studies showed that the ACC played a key role in selective attention, motor function, and emotional processing. However, little is currently known about how the ACC system is disrupted by TBI. Statistical analysis showed that the Stroop task was better at discriminating between TBI and control groups than other neuropsychological tests were [17]. To our knowledge, no neuroimaging studies on TBI patients performing the Stroop task have been published to date.

In this fMRI study, we tested our hypothesis that ACC dysfunction contributes to cognitive impairment in individuals with TBI. To this end, we compared the patterns of cortical activation during the Stroop task in TBI patients and healthy subjects.

Methods

Participants

The study population consisted of five patients, three men and two women aged between 24 years and 38 years (mean 29.8 ± 6.4 years), who were making a good neurological recovery after sustaining a severe closed head injury caused by motor vehicle accident. Severe head injury was defined as an initial Glasgow coma scale (GCS) score between 3 and 8 [18]. Initial MRI revealed small focal and diffuse neuropathological consequences, typical of moderate-to-severe TBI, in all patients. There was no evidence of massive contusions, including to the ACC, and none of the patients underwent surgical procedures. All underwent neuropsychological testing by the 30-point mini-mental state examination (MMSE) [19], the Wechsler adult intelligence scale-revised (WAIS-R) [20], and the Wechsler memory scale-revised (WMS-R) [21]; all tests were the Japanese-language version. A trained neuropsychological technician, blind to the MRI findings, administered the neuropsychological tests. These tests and fMRI were performed between 1 year and 7 years after the injury. Clinical and neuropsychological data are summarized in Table 1. Patients were compared with 11 age-matched and education-matched right-handed healthy subjects, seven men and four women aged between 23 years and 35 years (mean 28.1 ± 4.7 years). All control subjects were screened to ensure that they had no history of neurological damage or color-blindness. Written prior informed consent, approved by the Gifu University Medical Review Board, was obtained from all study subjects before inception of this investigation.

Task and design

We used a modified Japanese-language version of the Stroop test. The following two variants of the Stroop task were assigned [13]: (1) the color-naming Stroop task, in which the displayed word named the ink color of the word, and selected name color cards (e.g., the word "yellow" printed in green selects the green card); (2) the word-naming Stroop task, in which the displayed word named a color that was different from that of its ink color, and selected name color cards (e.g., the word "blue" printed in red selects the blue card). The colors used were red, blue, green, and yellow. The stimuli were shown by fiber-optic glasses (Silent Vision 4000, Avotec, USA). Each stimulated block consisted of 15 trials, presented at a rate of one trial every 2 s. The subjects responded by pressing right/left buttons in response to color-congruent/word-congruent targets [12]. A scanner was used to obtain accuracy data for all subjects. We were not able to record reaction time data during scanning.

Functional MRI procedure

We used a blocked fMRI design that involved presentation of a 30-s rest condition followed by a 30-s activation condition. This cycle was repeated three times over the course of 3 min. The resting baseline reference task was a standard condition during which subjects were instructed to lie still and remain quiet with their eyes open [22]. Functional and anatomical imaging was performed on a 1.5 T clinical scanner (Signa, GE Medical Systems, Milwaukee, Wis., USA) with a standard head coil. Blood oxygenation level-dependent (BOLD) functional images parallel to the bicommissural plane were acquired with single-shot echo planar sequences (repetition time 3,000 ms, echo time 50 ms, flip angle 90°, acquisition matrix 64×64, field of view 24 cm, 15 slices, slice thickness 7 mm, slice gap 1.5 mm). In addition, high-resolution T1-weighted three-dimensional spoiled gradient echo (SPGR) anatomical images were obtained (repetition time 7.2 ms, echo time 1.5 ms, flip angle 10°, acquisition matrix 256 ×256, field of view 24 cm, 160 slices, slice thickness 1 mm). During each cognitive task condition, 60 images per slice were acquired in 210 s (total = 960 images).

Table 1 Subject characteristics (*FSIQ* full-scale intelligence quotient, *VIQ* verbal IQ, *PIQ* performance IQ, *NA* not available)

Characteristic	TBI patients							Controls (n = 11)		*P*
	1	2	3	4	5	Mean	SD	Mean	SD	
Age/gender	28/F	24/M	38/F	35/M	24/M	29.8	6.4	28.1	4.7	0.78
Education (years)	14	12	12	16	14	13.6	1.7	14.6	1.3	0.73
Time to test (months)	54	12	24	84	48	45.6	28.7	NA	NA	
MMSE[a]	30	25	29	30	30	29.8	0.5	NA	NA	
WAIS-R										
FSIQ	86	70	100	90	65	82.2	14.5	NA	NA	
VIQ	85	86	89	93	73	85.2	7.5	NA	NA	
PIQ	91	57	114	88	65	83.0	22.6	NA	NA	
WMS-R										
Logical memory	84	54	93	65	62	71.6	16.3	NA	NA	
Attention	82	87	92	102	82	89.0	8.4	NA	NA	
Visual reproduction	69	69	88	65	69	72.0	9.1	NA	NA	
Stroop[b]	78	80	76	82	71	77.4	4.2	98.0	1.6	0.51

Data analysis

Post-processing was done on a Microsoft workstation using SPM99 (The Welcome Department of Neurology, University College London, UK) implemented in Matlab (Mathworks, Sherborn, Mass., USA). Realignment for motion correction, normalization, and deformation was performed by using the standard brain template from the Montreal Neurological Institute (MNI) and converting to the space of the stereotactic atlas of Talairach and Tournoux [23]. Smoothing was at 10-mm thickness; for data analysis we used thresholds of $P < 0.05$ (corrected) for individual subjects.

Using these data we calculated group activation maps by pooling the data for each condition at thresholds of $P < 0.001$ (uncorrected). The output from each statistical analysis is a statistical parametric map or a three-dimensional image.

Results

Behavioral data

Control subjects and TBI patients did not differ significantly with respect to gender, age, and years of education. Although the TBI patients did generally as well as the control subjects, they manifested a poor memory for recent events and had trouble with their jobs. Although the patients were able to perform the Stroop task, they made more errors than the controls; however, there was not a significant difference between the two groups ($P = 0.51$).

Imaging data

Follow-up MRI scans showed cerebral abnormalities in two patients. Patient 4 in Table 1 had a small contusion scar at the bilateral frontal cortices and patient 1 had a slight subdural effusion in the right frontal region. There was no evidence of abnormalities in the other three patients.

The location of significant increases in the BOLD signal during the modified Stroop task is shown in Table 2 and Fig. 1. In TBI patients and controls, cortical activation was found in similar regions of the frontal [Broadmann's area (BA) 6, 44, 46], occipital (BA 19, 37), and parietal (BA 7, 40) lobes and resembled the patterns of activation documented in previous neuroimaging studies of the Stroop task in healthy non-Japanese controls [12, 13, 15], indicating that our modified Japanese version of the computed Stroop task can be used to evaluate cerebral recruitment in Japanese subjects.

As shown in Fig. 2, compared to the control group, the TBI group displayed more relatively decreased cerebral activation in the ACC (BA 32).

Discussion

Using fMRI studies, we compared the pattern of cortical activation in patients with TBI and healthy control subjects. Although cognitive impairment may be subclinical and discrete in TBI patients, it can pose considerable challenges in their social re-integration [1]. Our results provide results of our interrogation of cortical physiology after head injury.